Hybrid System of Systems Control : the TOKAMAK scenario

Claudia Corradino

Supervisor: Prof. L. Fortuna

Advisor: Prof. A. Buscarino

Dipartimento di Ingegneria Elettrica Elettronica ed Informatica
Universita' degli Studi di Catania

Doctor of Philosophy in Ingegneria dei Sistemi, Energetica, Informatica e delle Telecomunicazioni

October 2017

Acknowledgements

This thesis is partially supported by the EUROFUSION Consortium within the Contract of Association ENEA-UNICT, and by an AFOSR grant no. FA9550-13-1-0136.

Abstract

The basic definition of System-of-Systems (SoS) is that of a large-scale integration of many independent, self-contained systems having the common aim of satisfying a global need. Under this perspective, lots of systems of systems can be found in several fields where a common final goal drives systems towards a final SoS state. In nuclear fusion research area, several examples of SoS applications can be made. From the integration of all the constituents of the TOKAMAK machines which work together to achieve a sustained nuclear fusion reaction, to the circuits made of active analogue components mimicking plasma behavior, to the neural networks made of connected units working together in order to predict plasma variables behavior. In this work, investigation of several SoS relevant in TOKAMAK scenario is performed and interesting results enhancing the plant capabilities provided. This thesis itself has been structured with a SoS-like structures where the integration of self-contained chapters is performed in order to satisfy the global goal that is improving TOKAMAK performances.

Table of contents

List of figures

List of tables

Chapter 1

Introduction

1.1 System of Systems

Nowadays, the "System-of-Systems" (SoS) approach is widely adopted to describe the emergence of phenomena in several different fields. Generally speaking, a SoS is a collection of sub-systems pooling their capabilities together to assemble a more complex system characterized by improved functionality and performance with respect to the sum of the single systems [1]. The elements of a SoS can thus be of any nature depending on the field of studies and the process under investigation. In other words, people, software, hardware, policies can all be elements of a SoS that, by interacting together by mean of specific relationships, produce a system-level result otherwise not reachable by the elements alone. In particular, each system has its own management, tasks and resources which are adapted to meet SoS goals[2]. SoS results include

system level qualities, properties, characteristics, functions, behavior and performance.[3].

Under this perspective, appears clear that SoS operate in several applications and are widely adopted in many different fields, starting from a circuit, made of integrated active and passive components, able to reproduce a specific dynamical behavior, to a neural network made of neurons connected together with the aim of predicting a relevant variable by optimizing some objectives for decision making ([4]). A SoS approach has been applied for modeling and understanding of the national transportation system [5], in sensors networks where each sensor device cooperates and collaborates with the others, in electric power grids where large-scale, complex, dynamical systems must operate in order to supply electrical energy to customers providing an emergent intelligent behavior. Industrial Internet of Things (IIoT) systems rely on the integration of systems and software engineering with processes supporting decision making thus requiring well suited IIoT framework architectures. Thus, IIoT can be considered as SoS and well suited architecture framework for SoS applications can be adopted [6]. In [7], a large scale Multinational Missile Defense System is developed as SoS where independent constituents work together in difficult environments against threats. A predictive control scheme for freeway systems is developed in [8] where the freeway system is divided into heterogeneous portions, called clusters, and each cluster is considered as a system and the overall freeway as a SoS. A review of modeling SoS behavior in terms of emergent behavior is provided in [9], where negative emergence is defined as the one to be suppressed and positive emergence as the one to elicit.

From the listed SoS applications it appears evident that one of the fields where adopting a SoS approach may help dealing with complex phenomena is nuclear fusion. In fact, in nuclear fusion reactors the coordination of the constituent systems is very complex thus requiring to opportunely design a well-defined SoS architectures for most of the issues related to that.

The most investigated nuclear fusion device is the TOKAMAK, a machine able to confine highly magnetic particles by mean of strong directed magnetic field lines [10]. Due to extreme working conditions plasma instabilities occurs leading to disruption and damages to the plasma facing components (PFCs). A SoS approach appears to be well suited to cope with the heterogeneous sub-systems interacting in TOKAMAK machines. In particular, one can think to adopt a SoS approach either at a global level or at a specific sub-level. A SoS approach at a global level relates to the performance of the overall nuclear fusion machine thus the final stable nuclear fusion state emerges as the result of the interactions among processes occurring in plasma,e.g., during the occurrence of plasma instabilities, processes resulting from plasma and PFCs interaction, software tools dealing with controlling and monitoring plasma variables, analogue models able to enhance plasma instabilities modeling. A SoS approach at a specific sub-level takes into account issues related to nuclear fusion experimentation whose solutions emerge from the interactions of subsystems, such as electronic devices, and software tools. Under this perspective, when dealing with a specific issue, a contribution to the global task of reaching optimal nuclear fusion performance is generated even at the global level thus affecting the emergent global plasma behavior.

1.2 TOKAMAK Scenario

In the last decades, the world-wide growing energy consumption have led to an heavy energy demand, making barely sufficient the available energy sources. In this perspective, a promising source able to face this challenging need guaranteeing inexhaustible, safe and environmentally-friendly energy production is represented by nuclear fusion. In fact, exploiting the principle behind the Sun power, nuclear fusion reactions releases energy from the loss of mass in the product of two hydrogen nuclei, thus exploiting the mass-energy $m-E$ equivalence $E = mc^2$, where c is the speed of light in vacuum.

In order to achieve fusion reactions, very tight temperature and pressure conditions have to be met. In particular, the colliding particles require high temperatures to overcome the repulsive force acting between them, thus increasing the difficulties in a stable plasma confinement. However, plasma confinement has to be preserved in order to observe self-sustained fusion reactions. A possible solution to confine highly magnetic particles can be the adoption of strong directed magnetic fields, but this requires the design of suitable devices such as TOKAMAKs. These devices consist in a toroidal chamber that confines plasma at high temperature by means of a strong toroidal and poloidal magnetic field. Nowaday, research on plasma behaviour inside fusion plants, and especially TOKAMAKs, is gaining increasing interest in the scientific community [10].

1.2.1 TOKAMAK

In 1950, Soviet scientists invented the TOKAMAK machine. Since a helical magnetic field is required in order to achieve a stable plasma equilibrium, the application of both a toroidal magnetic field (travelling around the torus in circles) and a poloidal magnetic field (travelling in circles orthogonal to the toroidal field)is needed. In a TOKAMAK, the toroidal field is produced by coils that surround the torus, and the poloidal field is the result of a toroidal electric current that flows inside the plasma[11]. This current is induced inside the plasma with a second set of coils, making the plasma as the secondary circuit of a transformer, a schematic is shown in figure 1.1.

The core of a TOKAMAK is constituted by a toroidal chamber and the inner side of the chamber must be maintained constantly in a vacuum state by a pumping system in order to have an ideal environment for the fusion, also called the vacuum chamber.

A toroidal current is essential to maintain an elongated toroidal system in equilibrium, besides its role in heating the plasma through ohmic dissipation; without the poloidal magnetic field that this toroidal current generates, there is a vertical instability of the plasma, drifting in the direction of elongation. The force driving this instability results from the interaction of the poloidal field coil currents and the plasma current.

For a given toroidal magnetic field, plasma pressure increases with toroidal current up to a limiting value. In present large TOKAMAKs currents of several MA are used, for conservative assumptions it should be in the order of 20-30 MA, but technology advances in the direction

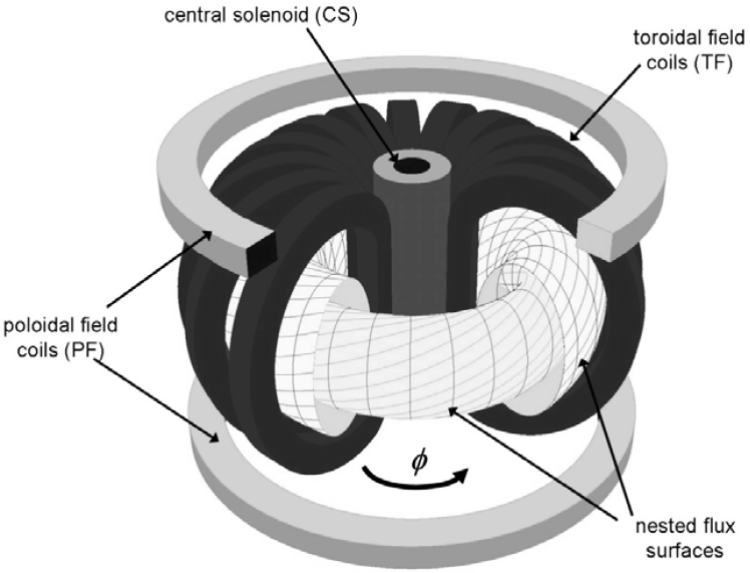

Fig. 1.1 Schematic representation of the magnetic field system of a TOKAMAK[12].

to lower this value.[11]

A pulsed machine TOKAMAK reactors are pulsed machines; in each pulse the plasma is created, ramped up to the reference flat-top current, heated, maintained in a constant state, and finally, cooled down and terminated. More specifically, a plasma discharge can be roughly divided into the following four different phases.

1. breakdown: this is the phase of formation of the plasma: the hydrogen gas in the vacuum vessel is ionized. The conditions for the breakdown are generally difficult to be achieved;

2. ramp-Up: during this phase, the plasma current, which is initially zero, reaches its desired steady-state value. Usually, the plasma current is linear or it has a singular non linearity during this phase. Also, the other plasma variables reach their nominal values;

3. flat-Top: during this phase, all the quantities that characterize the plasma should remain as constant as possible. This is the most important, and long phase, during which the production of energy should happen. Therefore, the control requirements are very stringent. Feedback control in this phase is very critical, since the plasma current and shape need to be continuously adjusted, and the disturbances that can happen must be rejected within a prescribed time;

4. ramp-Down: the plasma current and all the other quantities are driven to zero. The plasma is extinguished. [13]

Limiter and divertors Plasma is contained within a vacuum vessel and its interaction with the walls can produce intense local heating which can cause rapid erosion or even melting of the material composing the wall. Impurities in the plasma give rise to radiation losses and to dilution of the fuel. They are basically of two types; there are impurity ions coming from solid surfaces and secondly there are α-particles coming from the fusion process being then intrinsic in the reaction. Limiting their introduction inside the plasma is therefore

fundamental thus requiring a strategy to separate the plasma from the vacuum vessel. In this perspectives, two techniques have been developed; the first one consist of designing an outer surface boundary for the plasma,that is using a limiter, consisting of particular materials put in contact with the plasma itself as shown in figure 1.4. The second one is to magnetically drive particles following a particular shape in order to keep them away from the vacuum vessel by mean of a magnetic field divertor as shown in figure 1.4.

The main difference between the two technologies relies in the different position of the interaction of the plasma, with the divertor being far from the main chamber. This can give less contamination to the plasma, giving the possibility to work under better confinement state.

Plasma Instability In such extreme conditions, unstable phenomena are likely to occur in fusion plasma. In particular, one of the most dangerous is the Edge Localised Modes (ELMs) as they can harm first wall of the reactor chamber. ELMs are repetitive bursts of the plasma edge. Because of their periodicity, this phenomena can be thought as a single ELM cycle. The most rapid changes occur during an ELM crash which is usually significantly shorter than the time between the ELMs. ELM activity may evolve as a short, intense heat load on the wall leading to the erosion of the divertor or limiter materials. During the instability, the edge pressure gradient is reduced until the plasma becomes stable again. Then the pressure gradient starts recovering to the level where it reaches the stability limit so that another ELM occurs. If the conditions stay constant, the cycle can continue indefinitely.

Depending on the ELM type and the details of a plasma device, each ELM removes part of the plasma energy and particles.

The figure 1.6 shows the plasma cross-section and the radial plasma pressure profile at four different time points during an ELM crash. First the plasma is stable and has a steep pressure gradient at the edge. The gradient is maintained by the edge transport barrier that is always associated with the high confinement mode (H-mode) of tokamak operation. Then, pressure builds up at the plasma edge. The onset of an ELM can be imagined as an onset of many small turbulent eddies at the edge. The pressure collapses and the plasma is lost to the Scrape-Off Layer (SOL) where it flows along the magnetic field lines towards the divertor, whose plates produce a distinctive peak in the D-alpha radiation (visible light emitted by excited atoms of deuterium fuel). In order to decrease the divertor erosion and, at the same time, maintain a good control of the pressure profile, several methods of ELM suppression are considered at present. The two most promising approaches are the following pace making of ELMs by injecting small pellets of frozen fusion fuel into the plasma edge at a high frequency, see e.g. JET's capabilities in support of ITER and ELM coils for JET plasma edge ergodisation by resonant perturbations of the magnetic field. Studies at the DIII-D tokamak demonstrated an unexpectedly strong ELM suppression via resonant magnetic field perturbations. This is considered to be a very promising result for a reactor-relevant operation. Similar observations have been made at the ASDEX Upgrade tokamak.

Two of the most important TOKAMAK machines are Frascati TOKAMAK Upgrade (FTU) located in Frascati, Italy and Joint Euro-

pean TOKAMAK (JET) located in Culham,United Kingdom. These two TOKAMAKs are similar in the topology but different in scales and features.

1.2.2 FTU

The Frascati TOKAMAK Upgrade (FTU) is a medium size TOKAMAK operating since 1990, located at the ENEA Frascati, Italy. FTU is able to generate high density plasma by means of toroidal magnetic fields up to 8T and consequently, with plasma currents of the order of MA. The basic mechanical structure is provided by the monolithic toroidal magnet supporting the vacuum chamber and the poloidal field windings. The machine shown in figure 1.7 is contained in a cryostat, which is cooled by liquid nitrogen to limit the electrical power and energy requirements and to take advantage of the higher mechanical properties of the structural materials at cryogenic temperatures. The vacuum chamber is a compact, fully welded, stainless steel structure providing about 6270 cm^2 of access. The total height of the machine is 3 m, its overall diameter is 5 m and the total weight is 90 t. [14] The table 1.1 summarises the design parameters of FTU.

Table 1.1 Main FTU variables

Physical Characteristics	Value
Major plasma radius (m)	0.935
Minor plasma radius (m)	0.305
Toroidal magnetic field on plasma axis (T)	<8
Plasma current at q=2.5 (MA)	1.6

The main scientific objectives of FTU are the following:

- to study plasma transport at medium-high plasma density in the presence of strong additional RF heating;
- to test plasma heating and current drive by means of RF systems;
- to study plasma-wall interaction at high power loading;
- to study the influence of plasma profile control on plasma performance by means of pellet injection and different RF systems.

At the present time one of the main studies is focusing on plasma wall interaction using liquid metals, i.e. lithium and tin. The scientific aim of this program is to investigate and characterize liquid metal technologies to be applied for future TOKAMAK projects and in particular for the target plates of DEMO divertor.

Liquid Metals As introduced in the previous sections, at the strong temperature and pressure conditions needed to obtain fusion reactions, plasma instability phenomena, such as disruptions, are likely to occur, thus affecting plasma performance. Finding the appropriate material for the PFCs in TOKAMAK machines has been one of the main challenges of the nuclear fusion community. In fact, PFCs need to meet strict requirements in order to resist to the extreme conditions characterizing nuclear fusion reactions such as heat loads. It is known that plasma disruptions may be initiated by material particles release inside the fusion chamber, thus liquid metals have recently been reconsidered in the last decades. In fact, a PFC based on liquid metals do

not release material particles into plasma, on the other hand they may improve the quality of plasma by cleaning it from impurities.

Under this perspective, PFCs based on liquid metals have been deeply investigated in the last few years. In particular, two different liquid metals limiters have been tested in FTU, namely LLL and tin liquid limiter (TLL). Their structures are shown in Fig. 1.8. LLL has already been defined in the previous section: it is based on liquid lithium that being very reactive, cleans plasma facilitating oxidation phenomena over the limiter surface. Moreover, the main disadvantage in using this as PFC is its low boiling point preventing it to resist to high heat loads. On the other hand, tin boiling point is high thus allowing to sustain higher heat loads but, being not reactive, it may spreads impurities into plasma.

1.2.3 JET

Joint European Fusion (JET) was designed to operate in conditions relevant to fusion reactor, and its structure has been upgraded accordingly with the plasma physics findings, thus remaining a state-of-art for fusion technology. Nowadays, it is considered a fundamental test machine for the ITER technology.

JET is usually operated with deuterium fuel, leading to the generation of high magnetic fields (4T) and plasma current (5MA). The major and minor radii of the plasma torus are 3m and 0.9m respectively, and the total plasma volume is $90m^3$. JET adopts a topology based on a divertor as main plasma facing components in a vacuum vessel whose internal surface is covered by beryllium and tungsten tiles, which are able to cope with high heat loads. JET also has a flexible and pow-

erful plasma auxiliary heating systems, consisting of Neutral Beam Injection, Ion Cyclotron Resonance Heating and Lower Hybrid Current Drive. An extensive diagnostic suite of about 100 devices capturing a large amount of raw data per plasma pulse is available together with a high frequency pellet injector for plasma refueling and for the study of instabilities [15].

Physical Characteristics	Value
Major plasma radius (m)	2.96
Minor plasma radius (m)	1.25-2.10
Toroidal magnetic field on plasma axis (T)	3.45
Plasma current at q=2.5 (MA)	3.2

Table 1.2 Main JET variables

In this thesis, a SoS based approach will be used in three different contexts in order to deal with issues related to TOKAMAK machines. In particular, analogue SoS will be used in order to properly control emerging phenomena.
The remaining chapters will be divided as follow: in Chapter 2, analogue SoS is designed in order to dynamically model JET plasma instabilities taking into account non-ideal effects; in Chapter 3, different approaches based on SoS (neural network) are followed in order to predict thermal trend over the FTU limiter surface; in Chapter 4, spatio-temporal phenomena emerging from SoS are investigated focusing on the case of filamentary pattern formation occurring during

edge-localized-modes in JET; finally, in Chapter 5, the Conclusion of the overall work will be drawn.

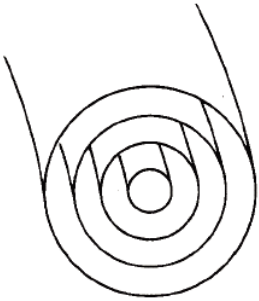

(a)

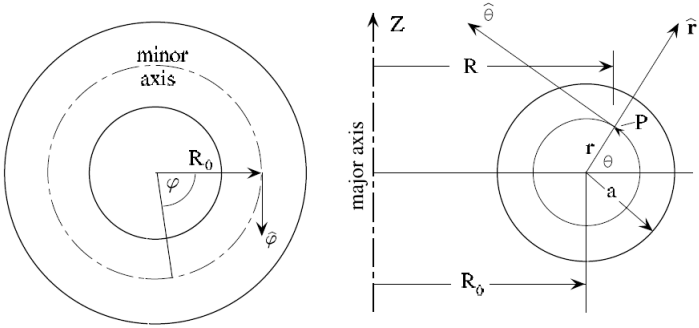

(b)

Fig. 1.2 (a) Desired plasma surfaces [16] - (b) System coordinates [11].

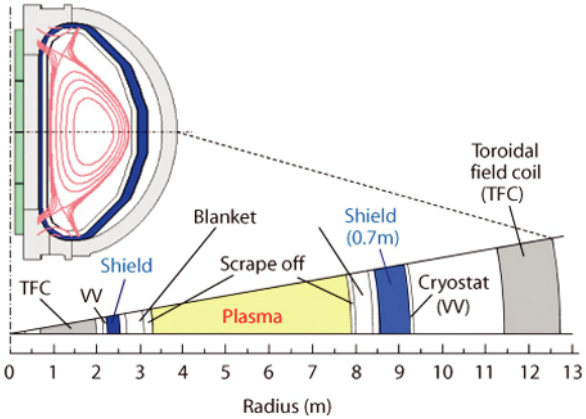

Fig. 1.3 General view of structure of a common TOKAMAK [17].

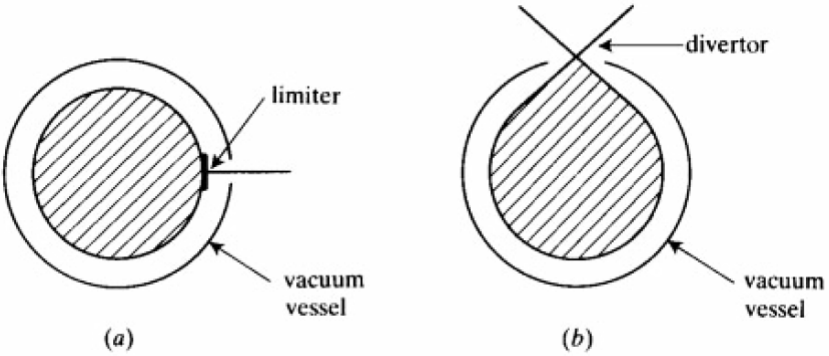

Fig. 1.4 Separation of plasma from the wall using (a) limiter (b) divertor [11].

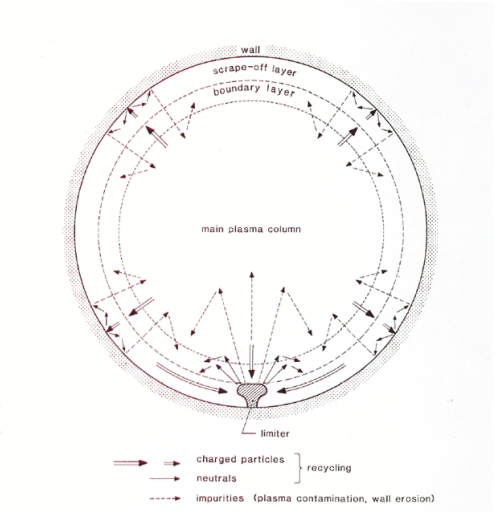

Fig. 1.5 Separation of plasma from the wall using limiter [16].

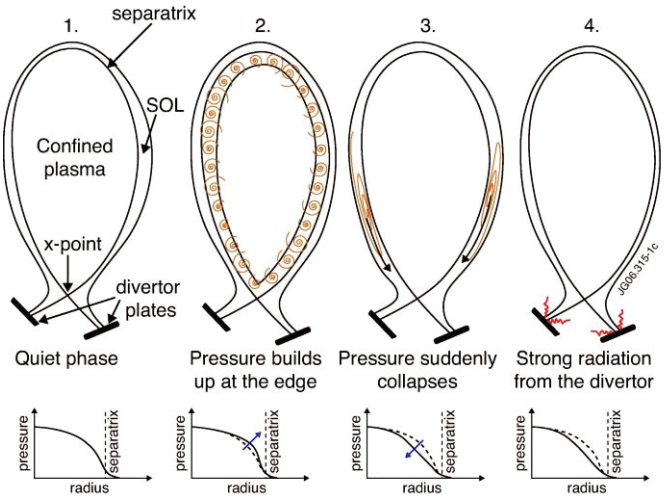

Fig. 1.6 Time development of an ELM crash [18].

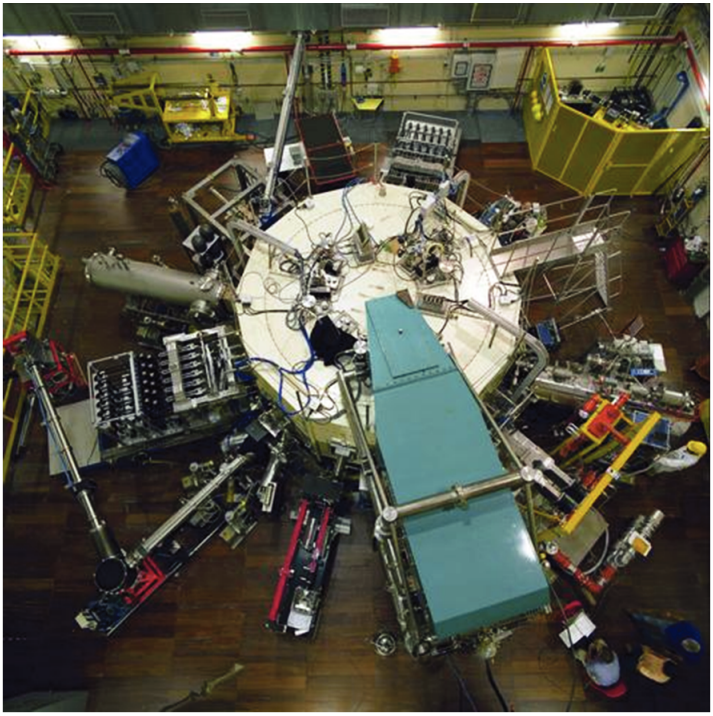

Fig. 1.7 FTU top view [16].

(a)

(b)

Fig. 1.8 The two limiters considered for experimentation: liquid (a) lithium and (b) tin limiters.

Chapter 2

Analogue SoS for Plasma Instabilities Dynamical Models

2.1 Introduction

Research about plasma behaviour inside fusion plants, and especially TOKAMAK, is gaining increasing interest in the scientific community. During last decades, several results on the modelling of dynamical behaviour in plasma have been presented. Among these, particular attention has been devoted to complex phenomena occurring in fusion plasmas during different types of instability. Plasma instabilities, in fact, are probably the most interesting phenomena affecting plasma performance, since their occurrence often leads to plasma disruptions and to the formation of structured patterns in the relevant measurements.

Plasma instabilities occurring during nuclear fusion experiments can be mainly classified in various types on the basis of the source of free energy driving them, such as density gradients, thermodynamic forces, anisotropy of the velocity distribution function, or interacting electric currents. The effects of relevant instabilities have been modelled in the last few years starting from observations and measurements acquired during fusion experiments. For instance, radiative collapse leading to disruption [19], multifaceted asymmetric radiation from the edge (MARFEs) [20], divertor heat flux asymmetries [21], the low-to-high (L-H) mode confinement transition [22], deterioration of confinement [23], and density limits [24]. Other instabilities often observed in fusion plasma are the Toroidal Alfve'n eigenmodes (TAE), triggered by neutral beam injection [25] and ion-cyclotron resonance heating [26], alpha-driven TAE modes [27], and fishbone modes [28]. Despite the abundance of mathematical model mimicking instabilities dynamics, a complete understanding of some of the most prominent phenomena occurring during their manifestation has not been achieved yet. In particular, diagnosing hot plasma behavioural aspects is still a challenging problem for the scientist dealing with nuclear fusion experiments. In this perspective, extensive experimental campaigns are necessary in order to collect the necessary datasets to derive comprehensive mathematical models. However, this approach may be time-consuming and expensive. The most straightforward alternative approach to investigate extremely hot plasma behaviour is to exploit analogies with hydraulic [29], mechanical [30], or electronic systems [31] whose models are defined according to similar mathematical relationships. Suitably designing analogue and re-scaled setups, it is possible to perform exper-

iments on these physical analogues, since such models can be easily implemented and characterized allowing a deeper understanding of some of the features representing plasma behaviours. However, it is not possible to realize a physical analogue which is exactly implementing a given mathematical model, since unavoidable source of nonideality are intrinsically contained in the device. The main motivation of this work takes origin from this consideration, trying to change a presumed drawback into an added-value. Nonideal behaviour is in fact likely to occur in fusion plasma processes and instability and may be strongly responsible to those actually observed phenomena still not captured by the model itself. Identifying the effective role of nonideal sources may be easier on analogue systems than in fusion plasma. The principal aim is, then, to apply the analogue system approach to implement the already known ideal plasma-related behavioural models and exploit the intrinsic nonidealities of the analogues to refine the ideal models.

Two cases will be investigated, the extension of the conservative system for gross modeling of plasma instabilities in TOKAMAK and the hybrid analogue model of ELM.

2.2 Extension of the conservative system for gross modeling of plasma instabilities in TOKAMAK

Mathematical models able to reproduce real fusion plasma behaviours give no definitive evidence of being capable to fully explain all their properties. Let us consider, as an example, the model described in [32]. It is based on the so-called Taylor - Couette (T-C) experiment, whose behaviour appears to be closely related to the that of toroidal

plasma devices. Exploiting this similarity and, under specific symmetry constraints, the principal qualitative features of instability occurring during ohmically heated TOKAMAK discharges, such as bursty and sawtoothing regime in TOKAMAK plasma, can be captured with a generic model based on ideal symmetry-breaking mode. The conservative model introduced in [32] has been originally used to mimic the occurrence of instabilities in the Joint European Torus (JET) fusion plasmas. It is worth to notice that the model reported in [32], such as many other models derived from experimental observation of instability processes, are essentially idealization of the real phenomenon. The main idea at the basis of this work come from the design of an electrical analog of the same plasma behavioural model. Even if the corresponding analogue electrical system can be easily implemented using common off-the-shelf circuit components, the implementation is affected by unavoidable linear and nonlinear dissipative effects related to the analogue devices adopted in the circuit. These devices introduce consistent deviations from the ideal conservative behaviour of the T-C experiment which cannot be eliminated. The resulting three dimensional dissipative mathematical model, which extends the conservative analytical model introduced in [32], shows oscillating and sawtoothing-like regimes, which however range from periodic to even chaotic bursting sequences. The onset of this complex phenomena has been demonstrated to be directly linked to the linear and nonlinear dissipative nonideal effects. This result may represent a further step towards a more realistic model of the plasma behaviour generalizing the conservative plasma gross behavior model. However, in order to validate this hypothesis the analogue implementation of the ideal model,

incorporating nonideal behaviours, has to be adopted to fine-tune parameters of the mathematical model in order to fit the data collected from real fusion plasma experiments and including the effects of noise and other nonideal behaviors that are always present in real systems. In this way, quantitative rather than just qualitative information about plasma phenomena can be obtained allowing a deeper knowledge on the actual linear and nonlinear behaviour of plasma during the occurrence of instabilities.

2.2.1 The dynamical model

Let us consider the following third-order autonomous dynamical system:

$$\begin{aligned} \dot{x} &= y - ax \\ \dot{y} &= \gamma x - Rx^3 + \Gamma z - by \\ \dot{z} &= \alpha - \beta z^2 - x^2 \end{aligned} \tag{2.1}$$

where a and b are positive dissipation rates and γ, R, α, β and Γ are system parameters. This system is an extension of the conservative system proposed in [32] for gross modeling of plasma instabilities in magnetic plasma confinement devices such as the TOKAMAK. In Eqs. (2.1), the dissipative terms ax and by are explicitly considered as well as a new feedback term Γz coupling the axisymmetric mode z to the second-order x-y dynamical system modeling instability amplitudes. An important parameter for the system is γ, considered here as the bifurcation parameter and allowing a numerical analysis of Eqs. (2.1). Choosing $a = b = 0.1$, $R = 1.09$, $\Gamma = 0.7$, $\alpha = 1$ and $\beta = 0.001$ gives the bifurcation diagram shown as blue in Fig. 2.1(a). For the range of γ

considered, there is always a period-1 limit cycle with constant amplitude, similar to the behavior reported in [32] where the axisymmetric variable z has no effect on the instability amplitude. Now consider a slight modification of Eqs. (2.1) including a further nonlinearity $F(x,\dot{x})$ given by

$$\begin{aligned} \dot{x} &= y - ax \\ \dot{y} &= \gamma x - RF(x,\dot{x}) + \Gamma z - by \\ \dot{z} &= \alpha - \beta z^2 - x^2 \end{aligned} \tag{2.2}$$

where the form of $F(x,\dot{x})$ sensibly affects the emergent behavior of the system in Eqs. (2.1). In particular, the first-order derivative of x gives the possibility of chaotic dynamics. When $F(x,\dot{x}) = x^3 - \delta\dot{x}x^2$, where δ is a further system parameter, the nonlinear function is the conjunction of two terms: a static nonlinearity x^3, and a product nonlinearity $\dot{x}x^2$ involving a square and a derivative operation. This modification corresponds to the explicit introduction of nonideal terms for two cascaded analog multipliers realizing the cubic operation in the previous section. Of course the $\dot{x}$ factor can be replaced by $y - ax$ to make Eqs. (2.2) formally autonomous.

For $\delta = 0.16$, the system in Eqs. (2.2) shows a bifurcation diagram with respect to γ that includes a cascade of period doublings towards a chaotic window shown as red in Fig. 2.1(a). Not shown in the figure is a region around $0.04 < \gamma < 0.08$ where a period-3 limit cycle coexists with the period-1 limit cycle. The three Lyapunov exponents shown in Fig. 2.1(b) confirm that the attractor is chaotic for $\gamma > 0.4$.

The attractor obtained for $\gamma = 0.45$ is shown in Fig. 2.2 projected onto the xy-plane. It has Lyapunov exponents given by $(0.0692, 0, -0.1406)$

and a Kaplan–Yorke dimension of 2.4921. Its basin of attraction is relatively small, bounded, and with smooth boundaries.

In the range of parameters considered, the occurrence of chaos is purely a consequence of the dynamical term $\dot{x}x^2$ in the nonlinear function F.

2.2.2 Nonideal effects in the analog multiplier

The most common nonlinearities in nonlinear (and in particular chaotic) oscillators are polynomials or the product of two state variables. For this reason, nonlinear circuits mimicking the behavior of the considered mathematical model usually require analog multipliers, either voltage [33] or current multipliers [34].

Off-the-shelf analog multipliers, such as the AD633 adopted in this work, are based on the four-quadrant multiplier [33]. However, it has been proved [35] that a static model is not sufficient to describe the input/output relationship of such multipliers. The dynamic model presented in [35] considers the memory effect involving time-derivatives of the inputs so that the output of the multiplier is given by

$$V_{out} = K(V_x(t)V_y(t) - T_A\dot{V}_x(t)V_y(t) - T_BV_x(t)\dot{V}_y(t)) \qquad (2.3)$$

where $V_x(t)$ and $V_y(t)$ are the two inputs, and K, T_A, and T_B are model parameters characteristic of the multipliers. The values of the model parameters can be estimated using the frequency-dependent analysis described in [35].

To implement polynomial nonlinearities, multipliers in cascade must be considered. In the case of a cubic term, two multipliers are

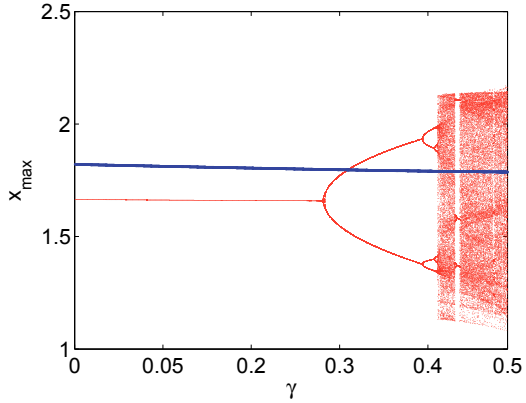

(a)

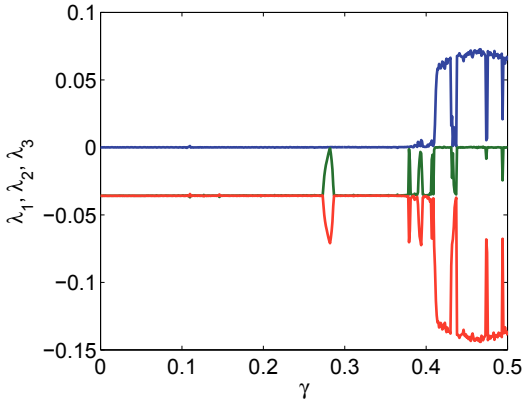

(b)

Fig. 2.1 (a) Bifurcation diagrams of system (2.1) (blue) and of system (2.2) (red) with respect to the bifurcation parameter γ. Local maxima of the state variable x are represented for each value of γ from 0 to 0.5. Other parameters are as indicated in the text. (b) Lyapunov spectrum for system (2.2) with respect to the bifurcation parameter γ, calculated according to the method in [36] for a total integration time $T = 10^7$ with step size $\Delta t = 0.01$. Other parameters are as indicated in the text.

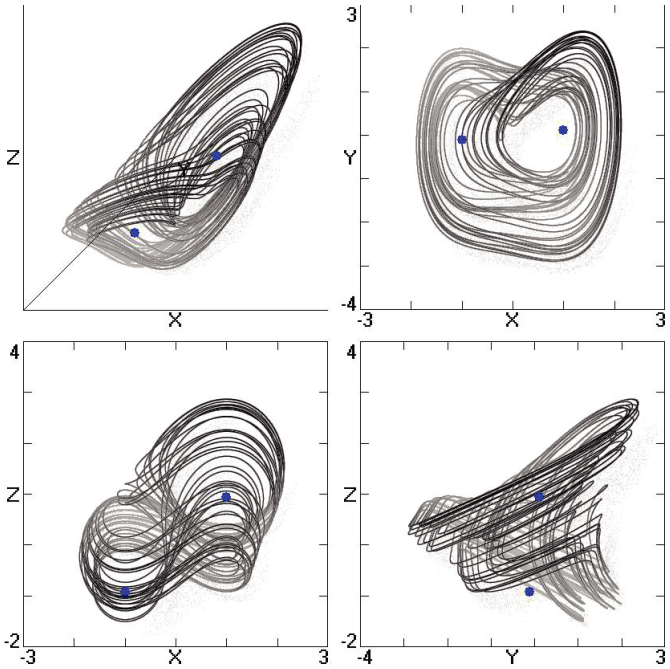

Fig. 2.2 Attractor for $a = b = 0.1$, $R = 1.09$, $\Gamma = 0.7$, $\alpha = 1$, $\beta = 0.001$, $\delta = 0.16$, and $\gamma = 0.45$. The two blue dots represent the saddle focus equilibrium points.

required. In the first, $V_x = V_y = x$ can be considered so that Eq. (2.3) becomes

$$V_{mult} = K[x^2 - T_A \dot{x}x - T_B x\dot{x}] \tag{2.4}$$

and then the output of the second multiplier connected in cascade with the first gives

$$V_{out} = K[V_{mult}x - T_A \dot{V}_{mult}x - T_B V_{mult}\dot{x}] \tag{2.5}$$

Expanding the previous equation and neglecting higher-order terms, the output of the two cascaded multiplier blocks is given by

$$V_{out} = K^2(x^3 - T\dot{x}x^2) \tag{2.6}$$

where K and $T = T_A + T_B$ are model parameters.

These parameters are frequency-dependent [35] and spoil the correct multiplication of the two input signals. In [35] the model parameters are estimated by applying a DC voltage at one of the inputs and a frequency swept sinusoidal signal at the other input. Estimates are derived from measuring the phase shift and amplitude response of the AC signals. Here a similar approach is adopted. The two cascaded multipliers are driven with a sinusoidal forcing signal at different frequencies, and the output is acquired using a NI-USB6255 data acquisition board with a sampling frequency $f_s = 400$kHz. Acquired data are then fitted to Eq. (2.6) using a symbolic regression algorithm [37] deriving the values of $K(f)$ and $T(f)$ for each frequency f.

Figure 2.3 shows the functional dependence of the model parameters on the frequency and indicates how the nonideal effects introduced by the multiplier are weighted. However, this characterization gives information only for the simple case in which the signals are periodic, and it is not sufficient for the design of chaotic circuits.

Chaotic signals are characterized by a broadband spectrum in a range of frequencies. Usually, chaotic circuits produce signals with frequencies as high as 10 to 60kHz, or more [31]. To derive a dynamical model of the analog multiplier that can be used for chaotic circuit design, the broadband nature of the signals must be considered. For this reason, the cascade multiplier have been characterized using input

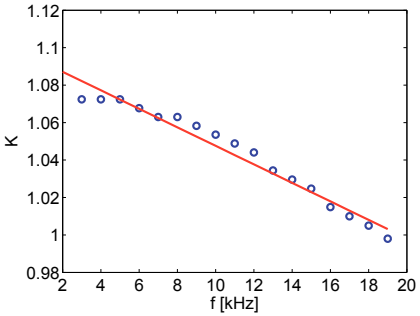

(a)

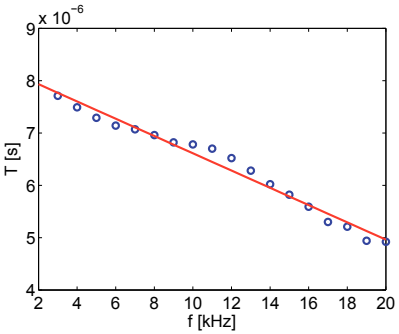

(b)

Fig. 2.3 Parameter estimation of the multiplier model using sinusoidal inputs: (a) K as a function of the frequency f of the input signal and a linear fit $K = -5 \cdot 10^{-6} f + 1.097$, and (b) T as a function of the frequency f of the input signal and a linear fit $T = -1.65 \cdot 10^{-10} f + 8.263 \cdot 10^{-6}$.

noise filtered with a low-pass filter with different cut-off frequencies. In Fig. 2.4 the functional dependence of the model parameters on the cut-off frequency is shown.

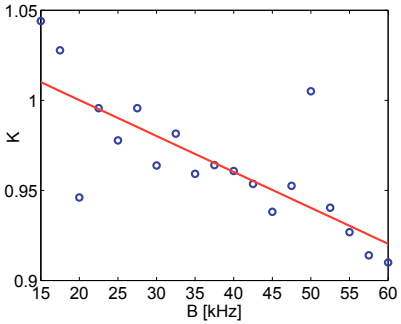

(a)

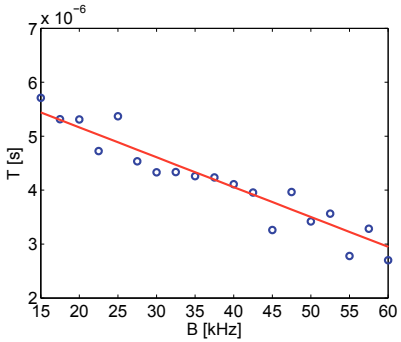

(b)

Fig. 2.4 Parameter estimation of the multiplier model using broadband signals: (a) K as a function of the bandwidth B of the noise input signal of the input signal and a linear fit $K = -0.002B + 1.04$, and (b) T as a function of the bandwidth B of the noise input signal and a linear fit $T = -5.56 \cdot 10^{-8}B + 6.274 \cdot 10^{-6}$.

The linear fits of the model parameters evaluated from the data allow temporal rescaling of the nonlinear circuits so that the nonideal behavior can be suitably exploited. In particular, the nonideal term

$T\dot{x}x^2$ can be considered in the design, allowing new chaotic dynamics to be realized without using additional circuit components, thus reducing the circuit complexity.

In the following, this approach is applied to design a new chaotic circuit in which the occurrence of strange attractors is purely a consequence of the nonideal term in the cascaded analog multipliers.

2.2.3 Circuit Implementation

The usual implementation of an analog circuit based on Eqs. (2.2) would involve a series of ideal components ranging from standard passive elements, i.e. resistors and capacitors, to active devices, such as operational amplifiers (OP-AMPs) to implement algebraic adders and integrators, and analog multipliers to implement the nonlinearities. Furthermore, the product involving a derivative would require a multiplier and an active differentiator block. While analog multipliers are often expensive, the differentiator can be realized using simple circuit elements but has intrinsic instability at high frequencies and a high sensitivity to noise due to the capacitive input.

The procedure described in Sec. 4.3 overcomes both problems, allowing a nonlinear circuit with only two analog multipliers to implement the whole nonlinear function $F(x,\dot{x})$. The other nonlinear terms can be realized by piece-wise linear (PWL) approximations implemented through standard diodes to avoid the occurrence of other nonideal terms. A circuit realizing the third-order nonlinear model in Eqs. (2.2) was designed and implemented with off-the-shelf components. In particular, the state variable approach in [31] was followed.

The designed circuit as shown in Fig. 2.5 uses OP-AMPs U1A, U8B and U2B to implement the active integrators made by a passive RC group and an algebraic adder, and the two cascaded analog multipliers U7 and U9 to realize the nonlinearity. OP-AMPs U11A and U13B allow the parameter γ to be adjusted, and OP-AMPs U10B and U12B together with diodes and resistors realize the square terms x^2 and z^2 as reported in [31].

The equations governing the circuit behavior are

$$\begin{aligned}
\dot{x} &= \frac{1}{R_{C1}C_1}\left[(\frac{R_{F1}}{R_1}-1)x+\frac{R_{F2}}{R_2}y\right] \\
\dot{y} &= \frac{1}{R_{C2}C_2}\left[-\frac{R_{F2}}{R_4}F+\frac{R_3R_{F2}}{R_{14}R_{15}}x++\frac{R_{F2}}{R5}z+(\frac{R_{F2}}{R6}-1)y\right] \\
\dot{z} &= \frac{1}{R_{C3}C_3}\left[\frac{R_{F3}}{R_{10}}V-\frac{R_{F3}}{R_8}x^2-\frac{R_{F3}}{R_9}\frac{R_{33}}{R_{32}}z^2+(\frac{R_{F3}}{R_7}-1)z\right]
\end{aligned} \tag{2.7}$$

The nonlinear function $F = x^3 - \delta\dot{x}x^2$ of Eqs. (2.2) has parameters fixed by a temporal rescaling according to Fig. 2.4. Comparing function F with Eq. (2.6), it is possible to derive relationships mapping the parameters of the cascaded multipliers to the circuit parameters such as $R = K^2\frac{R_{F2}}{R_4}$ and $\delta = \kappa T$, where κ is the temporal rescaling introduced as $\tau = \kappa t$. It follows that $K = \sqrt{R\frac{R_4}{R_{F2}}} = 0.93$, which according to Fig. 2.4(a) is the value obtained when the spectrum of the input signal has a bandwidth of 55kHz. Since the mathematical model has bandwidth of 1.1Hz a coefficient $\kappa = 50000$ has been introduced leading to a value of $T = 3.22 \cdot 10^{-6}$ as derived from Fig. 2.4(b). This implies an implemented value of $\delta = 0.16$.

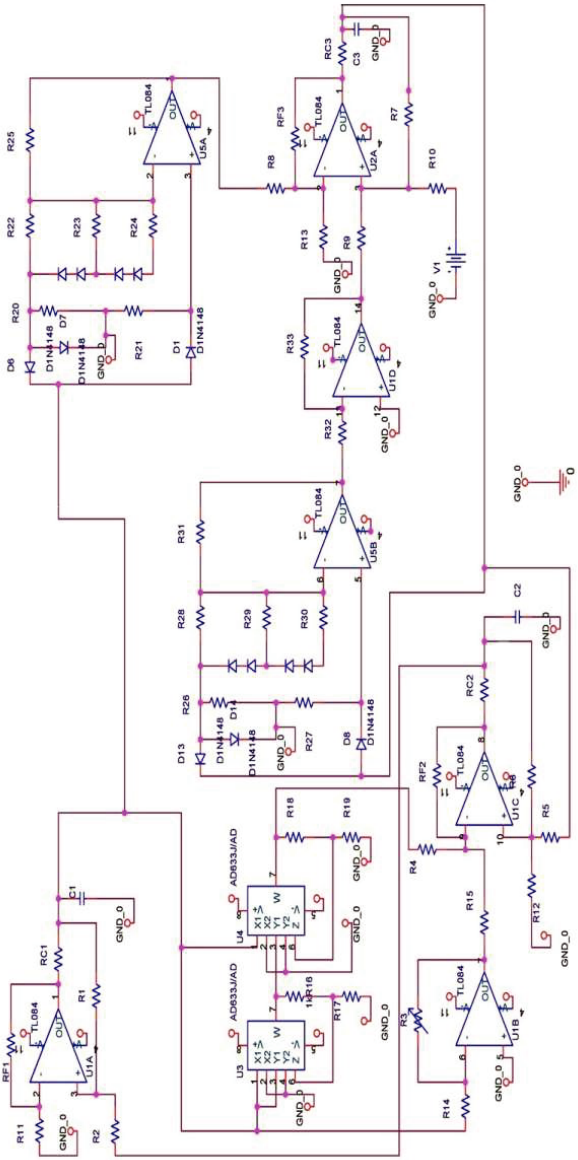

Fig. 2.5 Circuit implementation of the model.

Since the temporal scaling factor is given by

$$\kappa = \frac{1}{R_{C1}C_1} = \frac{1}{R_{C2}C_2} = \frac{1}{R_{C3}C_3} = 50000 \tag{2.8}$$

values of $R_{C1} = R_{C2} = R_{C3} = 2\text{k}\Omega$, and $C_1 = C_2 = C_3 = 10\text{nF}$ have been chosen.

The other circuit parameters are chosen so that (2.7) matches (2.2). In particular, $R_2 = R_7 = R_9 = R_{10} = R_{11} = R_{F1} = R_{F2} = R_{F3} = 100\text{k}\Omega, R_1 = R_6 = 112\text{k}\Omega, R_4 = 80\text{k}\Omega, R_5 = 142\text{k}\Omega, R_8 = 100\text{M}\Omega, R_{12} = 72\text{k}\Omega, R_{13} = 100\text{M}\Omega, R_{14} = 200\text{k}\Omega, R_{15} = 100\text{k}\Omega, R_{16} = R_{18} = 1\text{k}\Omega, R_{17} = R_{19} = 9\text{k}\Omega, R_{20} = R_{21} = R_{22} = R_{23} = R_{26} = R_{27} = R_{28} = R_{29} = 10\text{k}\Omega, R_{24} = R_{30} = 4\text{k}\Omega, R_{25} = R_{31} = 20\text{k}\Omega$, while R_3 is a $100\text{k}\Omega$ potentiometer.

Signals were acquired using a National Instrument (NI-USB6255) data acquisition board with a sampling frequency $f_s = 400\text{kHz}$, and the circuit behavior with respect to γ was analyzed. Figure 2.6 shows that the circuit follows the same route to chaos as the model in Eqs. (2.2) with a window of chaotic oscillation in good agreement with the predictions shown in Fig. 2.1a.

The attractor shown in Fig. 2.7 was obtained from the circuit with $\gamma = 0.45$ and agrees well with the simulated attractor in Fig. 2.2.

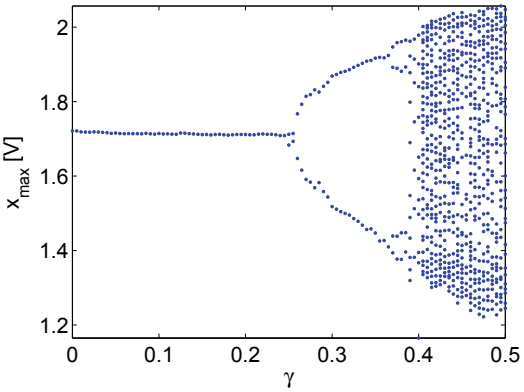

Fig. 2.6 Experimental bifurcation diagram with respect to the parameter γ shown in the local maxima of the state variable x.

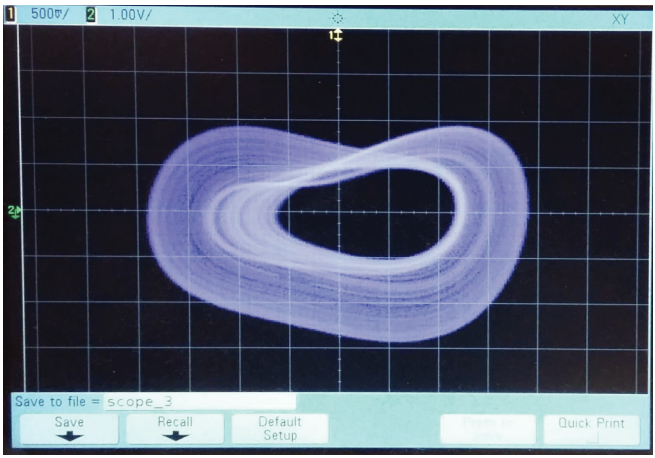

Fig. 2.7 Oscilloscope trace of the attractor on the xy-plane from the circuit with $\gamma = 0.45$.

2.3 The Hybrid Analogue Model of the Edge Localized Modes

Several models have been defined in order to reproduce the behavior of plasma related variables. Some of them [38] are aimed to determine the physical relationships which drive the instability process, while others are based on the identification of dynamical systems whose behavior qualitatively follows that observed in real experiments. In this paragraph, we will focus on the minimal model introduced in [39], which is based on two physical equations, related to plasma pressure and magnetic field, aiming at qualitatively understand large scale plasma instabilities resulting in periodic nonlinear plasma perturbation. It is a low dimensional model describing the quasi-periodic plasma dynamics observed in fusion experiments in Tokamaks is studied. In fact, understanding ELMs formation and evolution represents one of the main challenges in nuclear fusion research since these can damage PFCs due to their extreme high energy transfer rate.
A low-dimensional description of ELMs dynamics is fundamental to qualitatively understand the effect of changes in the driving parameters (e.g. heating power) allowing to design dedicated control strategies (e.g. pellet injection for ELM mitigation). Analyzing the main features of the plasma quantities by adopting an analogue model, in particular when instabilities occur, could be helpful in order to control the overall reaction and to set up the confinement time.

The hybrid analogue model is designed and implemented in order to deeply investigate plasma variables dynamical behavior in presence

of ELMs. In particular, the analysis of the system dynamics before and after pellets injection is performed and a control strategy designed in order to be able to suppress ELMs.

2.3.1 Low-dimensional Model of the single cell

The model introduced in [39] is essentially based on the interaction occurring between a driving process and a relaxation process, characterized by different time-scales. In particular, the model is composed by two equations, the first one describing the instability phenomena and the fast events due to instability growth, where the displacement of the magnetic field from equilibrium represents a relevant variable to be considered. The second equation describes the power balance at the pedestal during ELMs and models the pressure gradient behavior.

Thus, the normalized dynamical system is given by the following equations:

$$\begin{aligned} \ddot{\xi} &= (p-1)\xi - \delta\dot{\xi} \\ \dot{p} &= \eta(h - p - \beta\xi^2 z) \end{aligned} \tag{2.9}$$

where ξ is magnetic field, p is the pressure gradient and δ, η, β and h are system parameters. The choice of focusing on the pressure gradient is a simplification introduced in [39] since it is considered much more relevant with respect to the current gradient in presence of ELMs.

The corresponding dimensionless system of three first-order differential equations can be derived posing $x = \dot{\xi}$, $y = \kappa\xi$, and $z = p$, with κ a normalizing factor including also parameter β.

$$\begin{aligned} \dot{x} &= (z-1)y - \delta x \\ \dot{y} &= x \\ \dot{z} &= \eta(h - z - y^2 z) \end{aligned} \tag{2.10}$$

This model is able to qualitatively describe different dynamical behaviors depending on the value of three bifurcation parameters, namely h, η and δ. In particular h is the power input normalized with respect to the critical value of the pressure gradient, η is a term representing the heat diffusion coefficient and δ is related to the dissipation/relaxation of perturbations related to ELMs bursts.

The definition of parameter h is given so that the instability phenomenon occurs above a given input power threshold, i.e. when $h > 1$, implying that the critical pressure value is reached. As a consequence, by setting $h = 1.5$, i.e. so that instability can take place, and varying η and δ different dynamical regimes can be observed. In particular, for very low values of η, ELMs type oscillations appear as characterized by a slow-fast dynamics, with long rise time and short crash time.

Numerical integration of Eqs. (3.13) with $h = 1.5$, $\delta = 0.5$, $\eta = 0.01$ are reported in Fig.2.8, in which the three variables are plotted. In particular, the trend of z, i.e. the pressure gradient, resembles the typical behavior of the electron density measured in JET experiments during an ELM.

One of the strategies adopted in order to suppress ELMs is by injecting pellets as it was previously stated. In fact, pellets injection into the plasma can mitigate their occurrrences ELMs [39]. The modeling of such working condition is considered in [39] where a perturbation term is added in the first equation of the model 3.13:

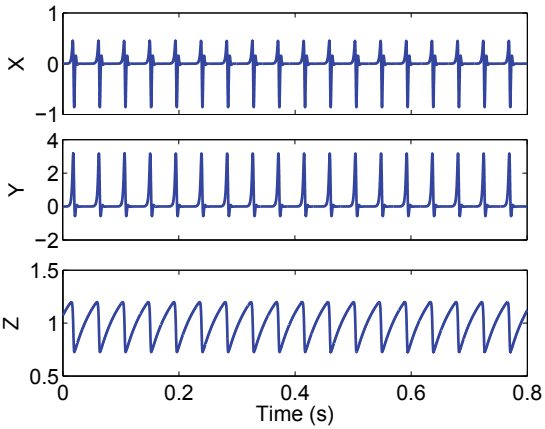

Fig. 2.8 Dynamical trend of $x(t)$, $y(t)$ and $z(t)$ when $\delta = 0.5$, $\eta = 0.01$ and $h = 1.5$.

$$\begin{aligned} \dot{x} &= -\{1-[z+P(t)]\}y - \delta x \\ \dot{y} &= x \\ \dot{z} &= \eta[h - zy^2 z] \end{aligned} \tag{2.11}$$

The perturbation P(t) simulates the pellet injection and can be selected in the form :

$$P(t) = a * exp\{-[t - t_{period}\ int(t/t_{period}) - \delta_P]^2/b\} \tag{2.12}$$

where a is the perturbation amplitude, t_{period} is the perturbation period, δ_P is the perturbation shift and b is the perturbation width. The

symbol "int" specify that the ratio must be integer.

The system parameters are set to work in the ELMs region: $h = 1.5$, $\delta = 0.5$, $\eta = 0.009$. Instead the perturbation parameters are chosen in the following way: $a = 5$, $t_{period} = 5$, $\delta_P = 2$ and $b = 2$.

The capability of the model to catch typical features of plasma measured quantities has been clearly discussed and assessed in [39].

2.3.2 Hybrid Circuit

Circuit design By adopting the same steps described in the previous section, the circuit design and implementation is performed in agreement with the model 2.11. Let us fix $C_2 = 220nF$, $R_{C2} = 2k\Omega$ and $R_{F2} = 100k\Omega$. The circuital equations are derived in 2.13

$$\begin{aligned}
\dot{x} &= \frac{1}{R_{C1}C_1}\left[\left(\frac{R_{F1}}{R_1} - 1\right)x - \frac{R_{F1}}{R_2}y + \frac{R_{F1}}{R_3}V^* + \frac{R_{F1}}{R_2}\frac{P(t)y}{10}\right] \\
\dot{y} &= \frac{1}{R_{C2}C_2}\left[\frac{R_{F2}}{R_4}x + \left(\frac{R_{F2}}{R_5} - 1\right)y\right] \\
\dot{z} &= \frac{1}{R_{C3}C_3}\left[\frac{R_{F3}}{R_7}V - z - \frac{R_{F3}}{R_6}V^{**}\right]
\end{aligned} \tag{2.13}$$

where $R_4 = R_{F2} = 100k\Omega, R_5 = R_{F2} = 100k\Omega, R^{**} = R_{F2} = 100k\Omega, R_7 = R_{F3} = 100k\Omega, R^{***} = R_6 = 10k\Omega$

The perturbation term is integrated in the circuit with an AD633 multiplier. Circuit parameters are chosen so that 2.13 matches 2.11. In order to have comparable frequencies with the perturbation the capaci-

tor values used in the circuit are set in the following way: $C_1 = C_2 = C_3 = 10nF$.

The overall analogue circuit implementation is shown in Fig. 2.9:

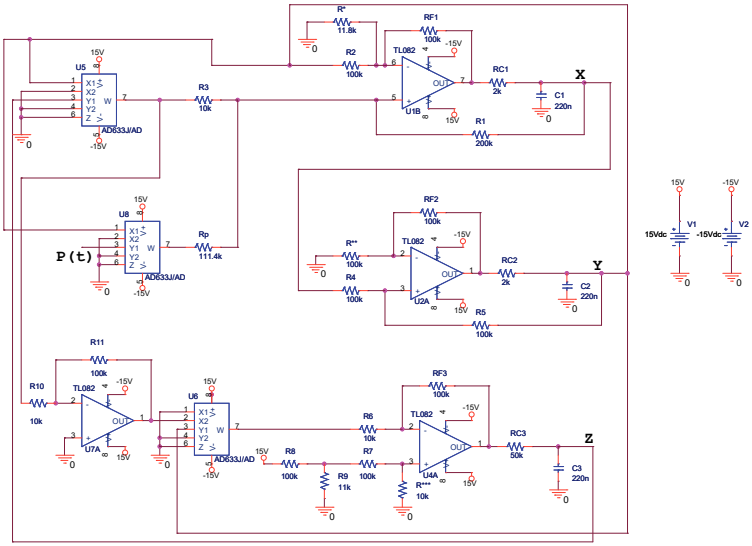

Fig. 2.9 Circuit implementation.

Perturbation implementation by using Arduino The perturbation P(t) is implemented by using the microcontroller board Arduino®Uno [40]. It is a robust multipurpose board, the most used and documented board of the whole Arduino®family. The microcontroller is programmed so that the perturbation is implemented and the result coded as an 8-bit word and sent to the circuit by means of the digital

output of the board.

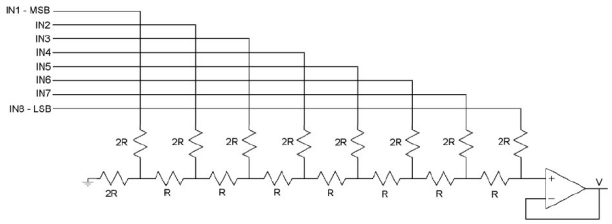

Fig. 2.10 Electrical scheme of the R-2R converter.

The digital to analog converter is implemented utilizing a R-2R converter with an output buffer [41]. R is equal $10k\Omega$ and the buffer is an operational amplifier TL084. The power supply is a dual voltage equal to $\pm 15V$.

2.3.3 Results

The sampling frequency is equal to $f_s = 150kHz$. The two cases , before and after pellets injection are analyzed. In particular, in figure 2.11 the dynamical trends of plasma variables in ELMs conditions are shown by using both simulations and experimental results. As it can be noticed, the dynamical behavior is quasi-periodic as it is supposed to be during ELMs occurrence in real nuclear fusion experiments. Once pellets injection is activated, the dynamics of the system become chaotic and the ELMs are suppressed as it is shown in Fig. 2.12 where the behavior of the z variable is shown. The obtained results agree with the known literature stating that the dynamics of plasma variables during ELMs suppression is chaotic [42, 43].

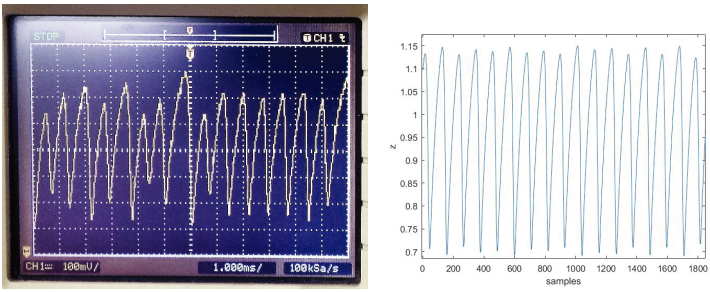

(a) (b)

Fig. 2.11 Experimental trend of z variable before pellet injection.

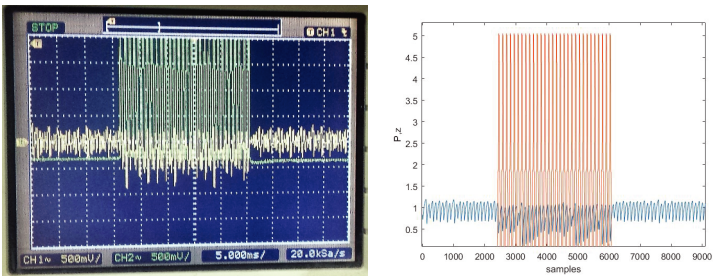

(a) (b)

Fig. 2.12 Experimental trend of ELMs with pellet injection. Perturbations P(t) are shown by green lines in the case (a) and by red lines in the case (b).

The attractors for both the situations are shown in Fig. 2.13 and Fig. 2.14. Thus, the applied external perturbation changes the plasma variables dynamical regime and increases ELMs frequency.

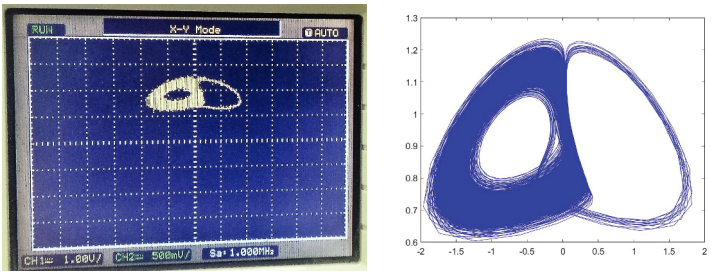

(a) (b)

Fig. 2.13 Experimental trend of the attractor on the zy-plane before pellet injection.

The t_{period} parameter space has then been explored- In fact, t_{period} in the perturbation expression 2.12 affect the frequency of the signal as it can be noticed in Fig. 2.15 is shown the case with $t_{period} = 35$:

As a consequence, increasing the t period, the frequency of the perturbation signal decrease thus leading to a more slighter effect on the ELMs.

The bifurcation diagram as a function of t_{period} is shown in 2.16 where it can be noticed that for higher t_{period}, ELMs region is characterized by limit cycle because pellet injection has lower effects on their dynamics. On the other hand, for lower t_{period} the system behaves chaotically because the pellet injetion higher affects ELMs thus sup-

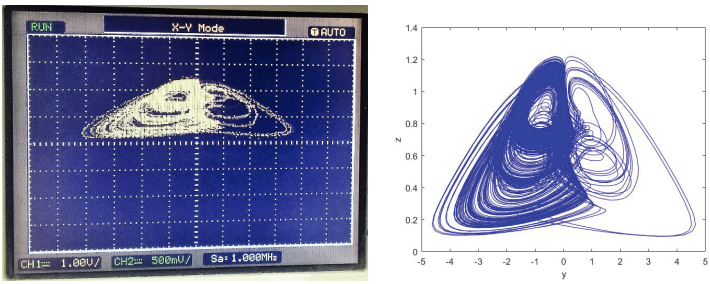

(a) (b)

Fig. 2.14 Experimental trend of the attractor on the *zy*-plane after pellet injection.

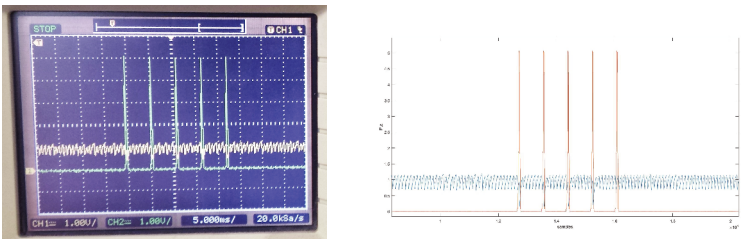

(a) (b)

Fig. 2.15 Experimental trend of ELMs with pellet injection by varing the parameter t_{period}. Perturbations P(t) are shown by green lines in the case (a) and by red lines in the case (b).

pressing them.
As expected the numbers of minimum points decrease with the increase of the t_{period}.

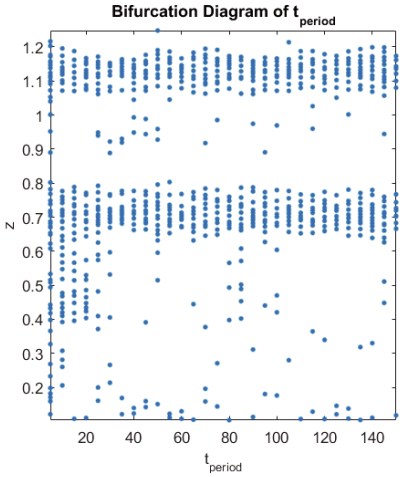

Fig. 2.16 Experimental bifurcation diagram with respect to the parameter t_{period}.

2.4 Conclusion

The realization of reliable nonlinear electronic circuits for modeling complex phenomena and exploring their behavior is a fundamental topic in nonlinear science. In this chapter, the implementation of two analogue model mimicking two different kind of plasma instabilities occurring in TOKAMAK machines have been performed.

In the first paragraph, a new strategy to design nonlinear electronic circuits which exploits the intrinsic nonideal properties of analog multipliers is proposed. In particular, the nonideal behavior of two cascaded analog multipliers has been characterized by deriving a dynamical model which takes into account unavoidable memory effects introduced by the four-quadrant cell. The response of analog multipliers in the presence of broadband signals, such as chaotic oscillations, has been studied, unveiling the relationship between model parameters and the bandwidth of the input signals. To demonstrate the effectiveness of the proposed design scheme, a new chaotic circuit in which the nonideal terms of the analog multipliers play a crucial role in the onset of chaos is introduced. The guidelines for designing reliable nonlinear electronic circuits exploiting the unwanted nonideal behaviors of analog devices introduced in this work pave the way for the definition of a new class of nonideal chaotic circuits. The proposed circuit represents a new three-dimensional dissipative mathematical model which extends the conservative analytical model introduced in [32] by introducing a further feedback term. It represents the generalization of the so-called plasma gross behavior model introduced to mimic the occurrence of instabilities in the Joint European Torus (JET) fusion plasmas. During the last decades, significant effort has gone into deriving models that reproduce the behavior of the most relevant instabilities. The idea of incorporating nonideal behaviors can thus be adopted for fine-tuning such physical models. In the investigated case, the analogue implementation appears fundamental in order to enhance the mathematical plasma gross-behavioral model.

The same objective drove the second paragraph, where the need of controlling dangerous plasma instabilities ELMs have led to implement an analogue qualitative model that can be adopted to fine-tune the ideal physical model in time. In particular, an hybrid analogue model made of both an analog circuital part and a digital part has been designed able to model both the plasma variables during ELMs and after pellet injection. From the results, it has been possible to identify a parameter that can be adopted to control ELMs suppression by acting on pellets perturbations. The analog model implementation paves the way towards a more complex issue that is the modeling of the spatio-temporal phenomena occurring during ELMs. In particular, in the next chapter, a spatial extension of the previously investigated lumped parametric model will be performed in order to model the plasma edge phenomena emerging in TOKAMAK machines during ELMs.

Chapter 3

Modeling spatiotemporal complexity: analogue SoS for plasma instabilities spatio-temporal models

3.1 Introduction

In the previous chapter, the importance of analogue models implementation to catch non ideal dynamical behaviors of the plasma gross-behavioral model has been revealed. A part from the latter model, others have been formulated to mimic plasma variables dynamics during the occurrence of instabilities. In particular, one of the most investigated plasma instabilities is ELMs characterized by a peculiar trend in

time and space.

In this chapter, we propose a novel approach towards the qualitative modeling of spatiotemporal phenomena occurring in plasma during instabilities such as ELMs. The modeling strategy adopted is based on the representation of the pedestal area of the plasma torus by means of connected cells, following the paradigm of reaction-diffusion cellular nonlinear networks that has been widely adopted to model emerging spatiotemporal phenomena in complex systems.

This chapter is organized as follow : firstly we will focus on the general topic of modeling spatiotemporal complexity by using Reaction Diffusion Cellular Nonlinear Network (RD-CNN) and we will see an example of pattern formation (Turing patterns) from biology to show the impact of RD-CNN in modeling spatiotemporal phenomena; in the second part ,a detailed description of the plasma instabilities scenario and the characteristic spatiotemporal phenomena occurring during nuclear fusion experiments is provided, in particular the $2D$ dynamical model of a $N \times N$ RD-CNN considered to characterize the onset of spatiotemporal patterns during plasma instabilities is presented describing the motivations at the basis of the spatial extension of the model highlighting the relevance of the proposed model for the qualitative reproduction of the real behavior of relevant plasma variables during instabilities.

3.2 Emerging phenomena in Reaction-Diffusion Cellular Nonlinear Network

A useful SoS tool to model spatio-temporal phenomena is the reaction diffusion paradigm . In fact, this paradigm allows to investigate phenomena emerging from the dynamical interactions of spatially connected cells such as patterns formation.

In the last decades, the mechanisms leading to pattern formation in biology, chemistry and other science areas have been widely studied. The landmark in this field was given by Alan Turing in his seminal paper [44] on morphogenesis in biological organisms. Starting from these observations, the occurrence of patterns in spatially-extended systems has been intensively studied, focusing, among many other systems, on mechanical [45], electronic [46] and thermodynamic systems [47]. Phenomena related to pattern formation in biological systems are modeled by the interaction of chemicals called morphogenes through spatial biological arrays. These systems of spatially coupled nonlinear units can be modeled by means of a class of nonlinear differential equations, known as reaction-diffusion models, which are capable to exhibit the dynamics of pattern development. Each unit, which is usually referred to as a *cell*, is usually modeled as a two-dimensional system whose state variables represent two concentrations of morphogenes, one acting as activator and other as inhibitor.

The reaction process takes place locally in each cell: the activator reacts autocatalytically, along with the inhibitor, which inhibits itself, and the activator. This reactive process, however, is not sufficient to ensure pattern formation but a diffusive process acting on both

the activator and the inhibitor is also needed. The diffusion of the two species must occur in a way such that the activator diffuses at a smaller rate than the inhibitor. The different diffusion of morphogenes ensures that, eventually, a decrease of the activator takes place, thus providing long-range stability. This mechanism is responsible of the generation of a non-trivial, heterogeneous pattern in a system made of homogeneous, i.e. identical, cells. Diffusion processes occur in the presence of a gradient in the concentration of one morphogene that induces a flux of the same morphogene (self-diffusion) and/or of another chemical species (cross-diffusion). Although cross-diffusion is generally neglected in efforts to explain dissipative patterns in reaction-diffusion systems [46, 48], in many natural system it is shown to play a central role [49].

To carry out our analysis, an architecture based on Cellular Nonlinear Networks (CNNs) is considered because fits perfectly the structure of reaction-diffusion systems. In fact, CNNs have been widely used for the study of spatio-temporal phenomena (such as Turing patterns and autowaves) typically observed in reaction-diffusion systems, since they can map partial differential equations [46].

As concerns the cell nonlinearity, many works focused on the use of the Chua's diode or other operational amplifiers-based nonlinearities [46]. In this work, the memristor is used as nonlinear element with memory. This device now is gaining considerable interest from different scientific fields including digital and analog electronics and neuroscience [50]-[56]. Along with the resistor, inductor and capacitor, memristor is the fourth basic circuit element. Postulated in 1971 [57] and experimentally realized in the Hewlett-Packard laboratories after

three decades [50], it is a two-terminal electronic device displaying a functional relationship between the time integral of the current through it and that of the voltage across its terminals. Usually, its nonlinearity is modeled by piece-wise linear functions [51] or physics-based approaches [58, 59].

In this chapter, a CNN architecture is adopted in order to prove the onset of Turing patterns (TPs) in complex systems. In particular, two equivalent cells are considered: i) a circuit made of a capacitor, an inductor and an active nonlinear element, and ii) an equivalent Chua's oscillator with the memristor as the nonlinear element. We show that the structure may generate Turing patterns and derive the conditions for their onset in an analytical way.

3.2.1 The Cellular Nonlinear Network

The CNN consists of $M \times N$ basic cells diffusively connected. We first describe the basic cell and then introduce the equations for the whole structure. As the basic cell we can consider the two equivalent circuits reported in Fig. 3.1. Let us consider the memristor-based oscillator reported in Fig. 3.1(a), where M is a flux controlled memristor. The circuit is described by the following equations:

$$\begin{aligned} C_1\dot{v}_1 &= G(v_2 - v_1) - W(\phi)v_1 \\ C_2\dot{v}_2 &= -G_0 v_2 - G(v_2 - v_1) \\ \dot{\phi} &= v_1 \end{aligned} \tag{3.1}$$

where $G = \frac{1}{R}$, $G_0 = \frac{1}{R_0}$, v_1 and v_2 are the voltages across capacitors C_1 and C_2, respectively, and ϕ is the flux associated with the memristor. As in [51] we assume the following model for the memductance $W(\phi)$:

$$W(\phi) = \frac{dq(\phi)}{d(\phi)} \begin{cases} a & |\phi| \leq 1 \\ b & |\phi| > 1 \end{cases} \tag{3.2}$$

Model (3.1) can be rewritten in a more tractable form, by using the dimensionless variables $x = v_1/E$, $y = v_2/E$, $z = \phi/\phi_0$ (with $E = 1V$ and $\phi_0 = 1Vs$) and introducing the parameters $\alpha = -\frac{G}{C_1}$, $\beta = \frac{G}{C_2}$, and $\gamma = \frac{G_0}{C_2}$:

$$\begin{aligned} \dot{x} &= \alpha(-y + W(z)x) \\ \dot{y} &= -\beta(y - x) + \gamma y \\ \dot{z} &= x \end{aligned} \tag{3.3}$$

where

$$W(z) = \begin{cases} 1 + \frac{1}{G}a & |z| \leq 1 \\ 1 + \frac{1}{G}b & |z| > 1 \end{cases} \tag{3.4}$$

When $R_0 = -R$ in Fig. 3.1(a), we have $\beta = \gamma$ and Eqs.(3.1) reduce to:

$$\begin{aligned} \dot{x} &= \alpha(-y + W(z)x) \\ \dot{y} &= \beta x \\ \dot{z} &= x \end{aligned} \tag{3.5}$$

Observe that the same set of equations, namely Eqs. (3.5), also model the circuit of Fig. 3.1(b), made of three elements: a capacitor, an inductor, and a flux-controlled memristor. We note that this cell has been also used to build a CNN for generating autowaves [60]. However, in that case, the parameters of the isolated cell were designed

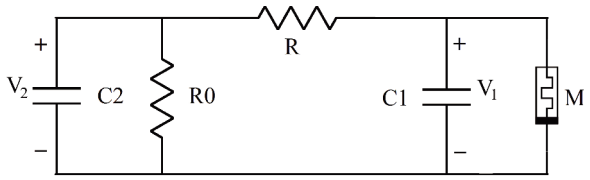

(a)

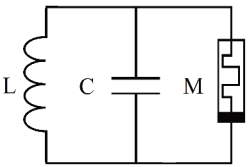

(b)

Fig. 3.1 Schematic representation of two memristor-based circuits: (a) Chua's oscillator with memristor; (b) memristor-inductor-capacitor circuit. When $G = -G_0$, both circuits are defined by model (3.5).

to obtain a limit cycle with slow-fast dynamics, whereas a totally different approach is adopted here.

Without loss of generality, in the following we normalize Eqs. (3.5) considering $G = 1$. Since $\dot{y} = \beta \dot{z}$, it follows that

$$z = \frac{y}{\beta} + c \tag{3.6}$$

where c is a constant term that takes into account the initial conditions of the memristor.

The normalized system now reads:

$$\begin{aligned}\dot{x} &= \alpha(-y + W(\tfrac{y}{\beta} + c)x) \\ \dot{y} &= \beta x\end{aligned} \tag{3.7}$$

The CNN is obtained by connecting the above cell into a grid of $M \times N$ cells, each one described by Eqs. (3.13). Each cell is diffusively connected to its four neighbors according to the following equations:

$$\begin{aligned}&\dot{x}_{i,j} = \alpha(-y_{i,j} + W(\tfrac{y_{i,j}}{\beta} + c)x_{i,j}) + \\ &+D_{11}(x_{i-1,j} + x_{i+1,j} + x_{i,j-1} + x_{i,j+1} - 4x_{i,j}) + \\ &+D_{12}(y_{i-1,j} + y_{i+1,j} + y_{i,j-1} + y_{i,j+1} - 4y_{i,j}) \\ &\dot{y}_{i,j} = \beta x_{i,j} + D_{21}(x_{i-1,j} + x_{i+1,j} + x_{i,j-1} + x_{i,j+1} - 4x_{i,j}) + \\ &+D_{22}(y_{i-1,j} + y_{i+1,j} + y_{i,j-1} + y_{i,j+1} - 4y_{i,j})\end{aligned} \tag{3.8}$$

where D_{11} and D_{22} represent the self-diffusion coefficients, while D_{12}, and D_{21} are the so-called cross-diffusion coefficients. Eqs. (3.15) represent a reaction-diffusion system based on Eqs. (3.13) with the more general form for diffusion, *i.e.,* the one including both self- and cross-diffusion. In the next Section, we show that, indeed, both terms are required to obtain Turing patterns in the structure.

For convenience Eqs. (3.15) are rewritten in a compact form by defining $f(x,y) = \alpha(-y + W(\frac{y}{\beta} + c)x)$ and $g(x,y) = \beta x$, and adopting the following notation for the two-dimensional discrete Laplacian:

$$\begin{aligned}\nabla^2 x_{i,j} &= x_{i+1,j} + x_{i,j-1} + x_{i,j+1} - 4x_{i,j} \\ \nabla^2 y_{i,j} &= y_{i+1,j} + y_{i,j-1} + y_{i,j+1} - 4y_{i,j}\end{aligned} \tag{3.9}$$

In this way, system (3.15) is written as

$$\begin{aligned} \dot{x}_{i,j} &= f(x_{i,j}, y_{i,j}) + D_{11}\nabla^2 x_{i,j} + D_{12}\nabla^2 y_{i,j} \\ \dot{y}_{i,j} &= g(x_{i,j}, y_{i,j}) + D_{21}\nabla^2 x_{i,j} + D_{22}\nabla^2 y_{i,j} \end{aligned} \tag{3.10}$$

In addition, in the following the partial derivative of the functions $f(x,y)$ and $g(x,y)$ appearing in the dynamics of the CNN will be denoted by $f_x = \frac{\partial f}{\partial x}$, $f_y = \frac{\partial f}{\partial y}$, $g_x = \frac{\partial g}{\partial x}$ and $g_y = \frac{\partial g}{\partial y}$.

The reaction-diffusion system (3.10) exhibits Turing patterns, that is diffusion-driven instability, when the equilibrium solution of the isolated cell is stable to small perturbations but unstable when diffusion is present. This principle can be translated into mathematical conditions by first considering the cell as isolated, linearizing the dynamics around its equilibrium and studying the stability of its equilibrium through the analysis of the Jacobian matrix. A first set of conditions is obtained by imposing that the equilibrium point is stable. Then, the effect of the diffusion is considered through a technique based on spatial eigenvalues and able to decouple the cell from the others. After that, the stability of the isolated linearized system is investigated. This time, the conditions on the parameters derived from imposing that the equilibrium point becomes unstable thanks to the presence of diffusion [61]. These conditions derived in [62] translate in Eqs. (3.10).

$$\alpha W(c) < 0 \tag{C.1}$$

$$\alpha\beta > 0 \tag{C.2}$$

$$D_{22}\alpha W(c) + D_{21}\alpha - D_{12}\beta > 0 \tag{C.3}$$

$$(D_{22}\alpha W(c) + D_{21}\alpha - D_{12}\beta)^2 - 4\det(D)\alpha\beta > 0 \tag{C.4}$$

$$\det(\mathrm{D}) = D_{11}D_{22} - D_{12}D_{21} > 0 \tag{C.5}$$

We remark that, if only self-diffusions are present, i.e. $D_{12} = D_{21} = 0$, because D_{22} is a positive coefficient, and conditions (C.1) and (C.3) cannot be simultaneously satisfied. Hence, in this case the instability must be driven by the cross-diffusion terms. Moreover, condition (C.5) appears because of the cross-diffusion terms. In fact $D_{12} = D_{21} = 0$ implies that $\det(\mathrm{D}) = D_{11}D_{22}$, which is positive by definition.

In order to give a circuit interpretation of the self and cross-diffusion coupling, let us consider the schematic representation reported in Fig. 3.2. It represents the nonlinear circuit model for a two-dimensional CNN having both self and cross diffusions. Resistors are used to implement self-diffusions, while cross-coupling is realized through the two port block transferring the current related to cross-diffusion terms to both dynamical equations (see Eqs. (3.15)).

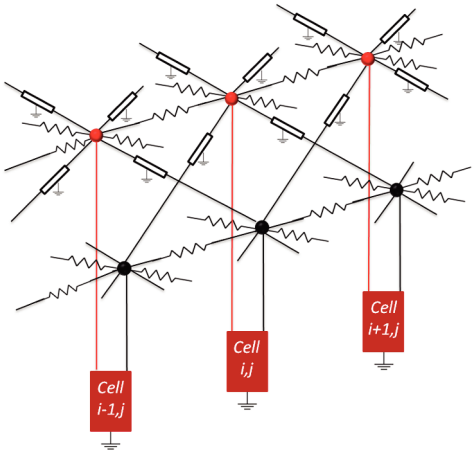

Fig. 3.2 Nonlinear circuit model for a two-dimensional Reaction-Diffusion CNN with both self and cross diffusion. Linear resistors with given conductance implements self-diffusion coefficients D_{11} and D_{22}, while the white two-port blocks implement cross-diffusion terms.

3.2.2 Numerical results

Numerical simulations of the CNN in Eqs. (3.10) have been performed considering $M = N = 100$. Without loss of generality, the initial conditions for the variables $x_{i,j}$ and $y_{i,j}$ were chosen to have a random uniform distribution between 0 and 1, and zero-flux boundary conditions are imposed.

Firstly, we discuss the simulations of a 100×100 CNN for a specific set of parameters, namely: $\alpha = 1$, $\beta = 0.8$, $D_{11} = 1$, $D_{12} = 4$, $D_{21} = 6$, $D_{22} = 26$, $a = -0.01$, $b = -0.61$, and four values of c ($c = 0$, $c = 0.2$, $c = 0.5$, and $c = -0.5$) are chosen. These parameters satisfy conditions (C.1)-(C.6). Similar results have been obtained for other sets of parameters satisfying these conditions. The results are shown in Fig. 3.3, where we observe Turing patterns in all four cases. We note that the value of c strongly influences the final pattern. In fact, by varying c, different structures can be observed ranging from stripes, mixed and spots/reverse spots patterns. From eq. (3.6), one gets $c = z(0) - \frac{y(0)}{\beta}$, so the parameter c accounts for the effect of the initial conditions of the memristor.

Clearly, the other parameters of the systems, the diffusion coefficients particularly, also affect the final state. Here, we illustrate the patterns obtained as a function of the ratio of self-diffusion coefficients $d = \frac{D_{11}}{D_{22}}$ and of the parameter c, keeping constant D_{12}, and D_{21}. In Fig. 3.4 a sketch of the different regions of the parameter space c-d is presented, when $\alpha = 1$, $\beta = 0.8$, $D_{12} = 4$, $D_{21} = 6$, $a = -0.01$, and $b = -0.61$. It is evident that for the same value of the memristor parameter c, different patterns emerge when d is varied. Interestingly, higher

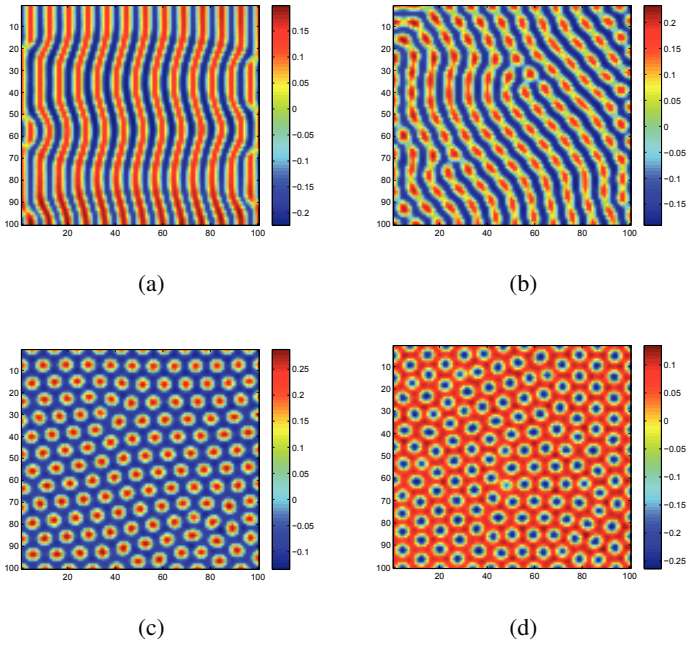

Fig. 3.3 Turing patterns generated from a 100×100 CNN as in Eqs. (3.10) in layer x, where c assumes four different values: (a) $c = 0$, stripes, (b) $c = 0.2$, mixture of stripes and spots, (c) $c = 0.5$, red spots in blue background, and (d) $c = -0.5$, blue spots in red background. The other parameters are fixed as: $\alpha = 1$, $\beta = 0.8$, $D_{11} = 1$, $D_{12} = 4$, $D_{21} = 6$, $D_{22} = 26$, $a = -0.01$, $b = -0.61$. Without loss of generality, initial conditions are taken randomly from a uniform distribution between 0 and 1, zero-flux boundary conditions are considered.

values of d lead to a wider c region, in which mixed stripe/spot patterns emerge, while lower values lead to a wider region of spot patterns.

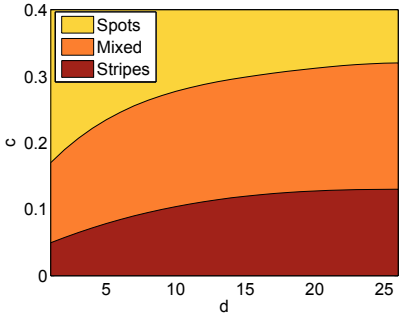

Fig. 3.4 Dependence of the type of pattern on the parameters c and $d = \frac{D_{11}}{D_{22}}$. Other parameters are fixed as $\alpha = 1$, $\beta = 0.8$, $D_{12} = 4$, $D_{21} = 6$, $a = -0.01$, and $b = -0.61$. Different colors indicate the emergence of stripes, spots, or mixed stripe/spot patterns.

The spatial wavelength of the emerging pattern may be related to the so called *average diffusion* [63], defined as the square root of the determinant of the diffusion matrix. In particular, if we define the critical wave number at the onset of Turing patterns as

$$\nu = \sqrt{\frac{\det(A)}{\det(D)}} \tag{3.11}$$

it follows that the critical TP wavelength is

$$\Omega = \frac{2\pi}{\nu} = \frac{2\pi}{\sqrt{\frac{\det(A)}{\det(D)}}} \tag{3.12}$$

As a consequence, if all parameters, except the cross-diffusion coefficients, are kept constant, patterns with different wavelengths may emerge. In fact, since $\det(\mathrm{D}) = D_{11}D_{22} - D_{12}D_{21}$, if $D_{12}D_{21}$ decreases,

then from Eq. (3.12) it follows that the spatial wavelength increases. Setting the parameters to $\alpha = 1$, $\beta = 0.8$, $a = -0.01$, $b = -0.61$, $D_{11} = 1$, and $D_{22} = 25.5$, different patterns with different values of c, D_{12} and D_{21} have been obtained as shown in Fig. 3.5. Observe that for both the stripes and spots patterns, the spatial wavelength decreases as $D_{21}D_{12}$ increases. It is important to remark that D_{12} and D_{21} have been set to satisfy conditions (C.1)-(C.6).

3.2.3 Conclusions

The occurrence of complex spatio-temporal phenomena in spatially-extended electronic circuits is a well-known topic in nonlinear electronics. The contribution presented in this section provides further insights by considering the use of memristive devices as non linear electronic elements and characterizing their role in Turing pattern formation. From an analytical perspective, the conditions under which Turing patterns can be observed in a CNN have been outlined, thereby providing a strategy for the design of memristive structures leading to complex patterns. Furthermore, the possibility to satisfy such conditions on the basis of the memristor state, i.e. its memory of past events, shows that pattern formation is definitely driven by the use of this peculiar nonlinear memory device. The proposed approach has focused on the generation of Turing patterns in 2D. However, it, and in particular Eqs. (3.10), may also be used to generate Turing patterns in 3D. To this aim, the Laplacian terms have to be generalized to include diffusion in the three spatial dimensions as described in [64].

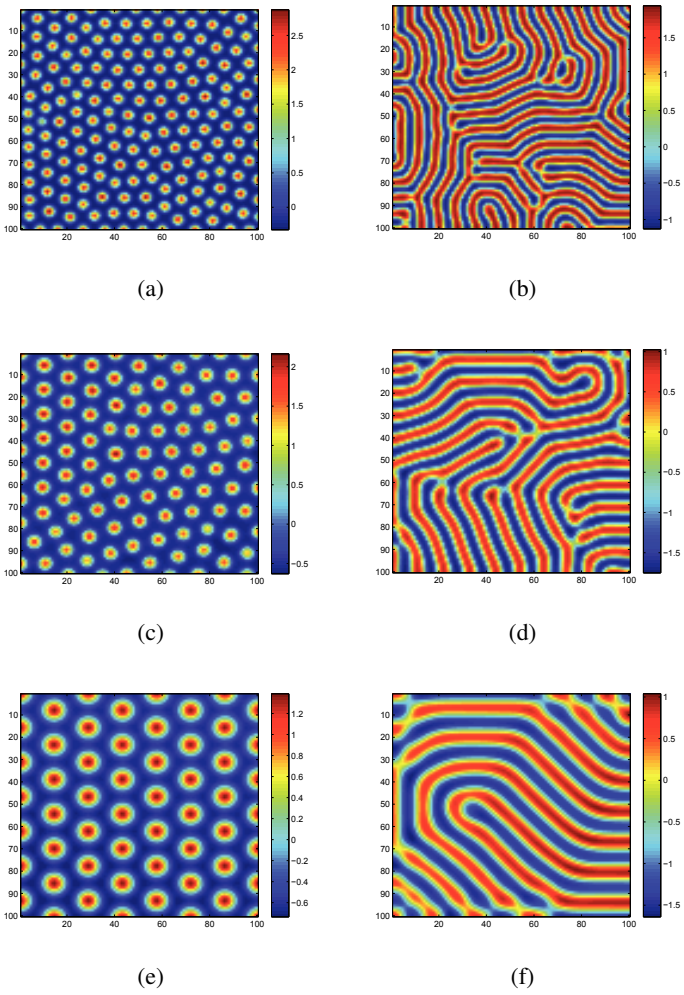

Fig. 3.5 Turing patterns generated from a 100×100 CNN on layer x obtained by fixing $D_{11} = 1$, and $D_{22} = 25.5$ and by varying $D_{21}D_{12}$ and c. (a) $c = 0.5$, $D_{12} = 4$, $D_{21} = 6$ ($D_{21}D_{12} = 24$), (b) $c = 0$, $D_{12} = 4$, $D_{21} = 6$ ($D_{21}D_{12} = 24$), (c) $c = 0.5$, $D_{12} = 3$, $D_{21} = 7$ ($D_{21}D_{12} = 21$), (d) $c = 0$, $D_{12} = 3$, $D_{21} = 7$ ($D_{21}D_{12} = 21$), (e) $c = 0.5$, $D_{12} = 1$, $D_{21} = 9$ ($D_{21}D_{12} = 9$), (f) $c = 0$, $D_{12} = 1$, $D_{21} = 9$ ($D_{21}D_{12} = 9$). Other parameters as indicated in the text.

In the next section, a similar approach will be followed considering the model describing plasma instabilities dynamics as elementary cell. In particular, the RD-CNN paradigm will be adopted to spatially extend this dynamical model.

3.3 Qualitative spatiotemporal model of the Pedestal Spatial Extension

One of the most important aspect in plasma physics is the capability of the TOKAMAK to magnetically confine plasma. In the 1980's a new operating mode has been described [65]. In fact, by increasing the heating power beyond a given threshold it has been observed that a bifurcation to a new confinement state, called H-mode, occurs leading to a dramatic increase in the plasma magnetic confinement. This was due to the formation of an insulating region at the plasma edge and steep gradient pressure that, besides the plasma confinement, leads to the occurrence of instabilities, such as the ELMs [65].Being characterized by the emission of a large amount of energy and particles towards the plasma facing components and, therefore, they can lead to damage and even disruptions. As a consequence, many studies have been devoted to better understand the behavior and the nature of these kind of instabilities in order to accordingly design suitable control strategies with the aim of avoiding their onset.

In the previous chapter, the analogue of the minimal model described in [39], which is based on two plasma pressure and magnetic field, has been deeply investigated and control strategy to suppress ELMs opportunely designed. This minimal model is a lumped parame-

ter model derived considering the portion of space of the pedestal as a unique domain in which the interaction occurring between the instability dynamics, modeled as a relaxation phenomenon, with the power balance dynamics, drives the system towards the onset of instability depending on global quantities. By using this dynamical model, the behavior of a complex plasma process can be described in terms of drive and relaxation, and therefore, two equations are considered, one related to the instability dynamics and one to power conservation. The model adopted in this work is therefore capable to generate nonlinear oscillations whose dynamics qualitatively resembles those typically observed during ELMs onset in the pressure gradient at the pedestal region, the edge of plasma region with significantly enhanced profiles gradient [66]. The analysis carried in [67] uncovered the rich bifurcation scenario that can be observed in the mathematical model, while in [39] the possibility to qualitatively reproduce dynamical behavior similar to that collected in real data has been investigated.

On the other hand, the occurrence of ELMs has been linked to the emergence of a complex spatiotemporal phenomenon consisting in *filaments* observable inside the vacuum vessel. In particular, formation of filaments has been already observed and characterized in MAST (Mega Ampere Spherical TOKAMAK), a TOKAMAK located in Culham, by means of a videocamera capturing images in the visible range [68]. Also in COMPASS (COMPact ASSembly), a TOKAMAK located in Prague, filaments have been characterized by means of specific probes capturing pressure gradient along the pedestal [69]. Aim of this contribution is to investigate the possibility to obtain a similar behavior in a 2D medium composed by locally coupled elements, each governed by

the minimal model reported in [39]. The 2D medium can be considered as a spatial discretization of the area of the pedestal, assuming that each small portion of space obeys to the dynamical equation of the qualitative minimal model.

The mathematical formalization adopted to describe the 2D medium follows the paradigm of RD-CNNs. This choice is motivated by the relative simplicity of the paradigm, which definitely represents a universal solver for partial differential equations. Several studies, in fact, adopt such approach to investigate emerging phenomena in spatiotemporal nonlinear domains [70, 62, 71].

3.3.1 Qualitative model of the filamentary pattern formation at the pedestal region

The well known qualitative dynamical model able to mimic plasma behavior during ELMs has been deeply analyzed in the previous chapter. The dynamical model is reported in Eqs. (3.13).

$$\begin{aligned} \dot{x} &= (z-1)y - \delta x \\ \dot{y} &= x \\ \dot{z} &= \eta(h - z - y^2 z) \end{aligned} \tag{3.13}$$

In this section, we aim to exploit this model to determine whether or not a coherent spatiotemporal behavior can emerge in a 2D medium representing a section of the pedestal region. As it is commonly known [70], pattern formation is strictly linked to the presence of a slow-fast dynamics, such that observed from the model behavior reported in Fig. 2.8. This consideration encourages us to follow this approach in order to find a region of the parameter space for the minimal model in

Eqs. (3.13), in which pattern formation can be observed. To clarify the plausibility of adopting the Reaction-Diffusion paradigm as approach to spatially extend the dynamic model of the single cell, let us focus on the origin of the third equation in (3.13), i.e. that representing the dynamics of the pressure gradient. It derives from the following equation governing the variation of the pressure gradient:

$$\frac{dp'}{dt} = \frac{1}{c_p} p' S D \tag{3.14}$$

where c_p is a scaling factor, S is the surface of the considered volume, and D is the diffusion coefficient. In this work, we considered the volume as partitioned in smaller portions, each regulated by the same equation, among which diffusion of the pressure gradient occurs.

A section of the medium resulting from this spatial discretization is investigated in order to study the possibility to obtain a filamentary structure, similar to that appearing in presence of ELMs. The section of the area at the pedestal is represented as a grid of $N \times N$ cells, each one connected with its four nearest neighbors and whose dynamics is described by Eqs. (3.13). The diffusive term, encompassing the coupling between cells, is included in the third dynamical equations according to the considerations made above.

The resulting system can thus be described by the following equations:

$$\begin{aligned} \dot{x}_{i,j} &= (z_{i,j} - 1) y_{i,j} - \delta x_{i,j} \\ \dot{y}_{i,j} &= x_{i,j} \\ \dot{z}_{i,j} &= \eta (h - z_{i,j} - y_{i,j}^2 z_{i,j}) + \\ &+ \bar{D} (z_{i-1,j} + z_{i+1,j} + z_{i,j-1} + z_{i,j+1} - 4 z_{i,j}) \end{aligned} \tag{3.15}$$

where $\bar{D}$ represents the normalized diffusion coefficient. Eqs. (3.15) represent a Reaction-Diffusion CNN system based on Eqs. (3.13).

For convenience Eqs. (3.15) are rewritten in a compact form adopting the following notation for the two-dimensional discrete Laplacian:

$$\nabla^2 z_{i,j} = z_{i-1,j} + z_{i+1,j} + z_{i,j-1} + z_{i,j+1} - 4z_{i,j} \tag{3.16}$$

In this way, system (3.15) is written as

$$\begin{aligned} \dot{x}_{i,j} &= (z_{i,j} - 1)y_{i,j} - \delta x_{i,j} \\ \dot{y}_{i,j} &= x_{i,j} \\ \dot{z}_{i,j} &= \eta(h - z_{i,j} - y_{i,j}^2 z_{i,j}) + \bar{D}\nabla^2 z_{i,j} \end{aligned} \tag{3.17}$$

The numerical simulations are performed considering the same set of parameters used in the previous section, thus $h = 1.5$, $\delta = 0.5$, $\eta = 0.01$, since we want to observe the spatiotemporal dynamics in presence of ELMs. As concern the diffusion coefficient we have considered different values leading to pattern formation. The results reported in the following are related to $\bar{D} = 0.5$, which, since the coefficient is normalized, represents an mean diffusion rate. Furthermore, a very important choice regards the boundary conditions. In fact, due to the fact that ELMs are governed by gradient profiles on the edge transport barrier, fixed boundary conditions have been applied to a RD-CNN with $N = 50$. Namely, the cells in the boundary are connected to a frame whose cells have states fixed to zero.

The spatial behavior of the pressure gradient z in the considered medium is reported in Fig. 3.6 for $T = 1$s, where the formation of propagating filaments similar to autowaves emerges. A qualitatively

similar representation can be obtained considering the central row of the $N \times N$ CNN and plotting the behavior of the pressure gradient as in Fig. 3.7. Here, the cells in the considered row reflects different radial positions, namely we plot the cells located at the edge of the medium representing the pedestal.

Furthermore, as observed in COMPASS TOKAMAK [69] the filamentary pattern emerging from profile gradient can be seen through plasma pressure gradient measurements, performed by specific probes. In particular, the values of the pressure gradient at different plasma layers of the pedestal can be measured, and then plotted as a function of the radial position over a string, determining a peculiar profile. Such profile assumes a characteristic decreasing behavior towards the edge of the pedestal region. The behavior of the RD-CNN reflects this structure, as reported in Fig. 3.8 where the value of the profile of the pressure gradient at $T = 5$s assumes a qualitatively similar behavior.

3.3.2 Conclusion

Modeling spatiotemporal phenomena occurring in the vacuum vessel of large TOKAMAKs is an highly interesting task. Furthermore, capturing the main features of the spatiotemporal evolution of plasma quantities during instabilities can be helpful in controlling their occurrence. This would lead to the improvement of the reactor performance and, consequently, to the increase of the confinement time towards ignition of self-sustained reactions.

In this chapter, we considered a model able to replicate the qualitative behavior of real observations of pressure gradient fluctuations during ELMs occurrence. We used such model as an elementary cell to

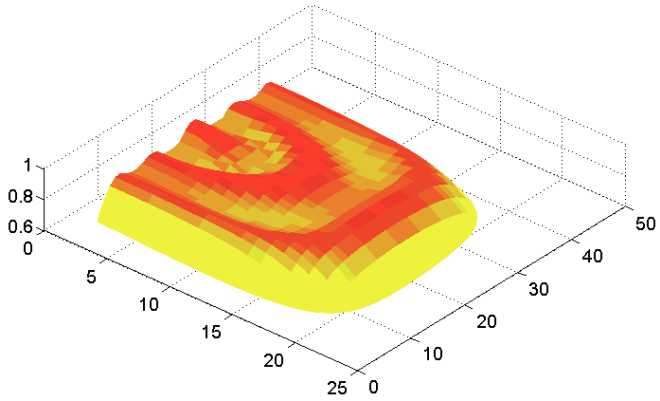

Fig. 3.6 Filaments formation in the two-dimensional RD-CNN: spatial distribution of the variable z when $\delta = 0.5$, $\eta = 0.01$, $h = 1.5$, $N = 50$ and $D = 0.5$. Here, the right part of the medium is reported.

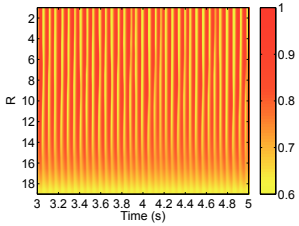

Fig. 3.7 Evolution of the pressure gradient along different layers of the simulated plasma torus as a function of time when $\delta = 0.5$, $\eta = 0.01$, $h = 1.5$, $N = 50$ and $D = 0.5$.

define a new spatiotemporal framework, which exploits the paradigm of RD-CNNs, aiming to reproduce the behavior of a section of the pedestal region. This has been done considering a spatial discretization

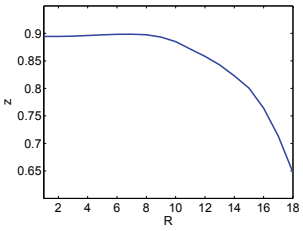

Fig. 3.8 Profile of the pressure gradient at $T = 5$s along different layers of the simulated plasma torus as a function of the radial position when $\delta = 0.5$, $\eta = 0.01$, h=1.5, $N = 50$ and $D = 0.5$.

of the area of interest assuming that each cell obeys to the dynamical equation of the global model. In this framework, a diffusion of the pressure gradient occurs and reveals to be fundamental in the formation of patterned structures. The investigation of such structures in the simulated medium allowed us to retrieve the characteristic behavior of filaments formation in real experiments during ELMs, namely the peculiar pressure profile with respect to different radial positions toward the edge.

The results obtained and discussed in this chapter are merely qualitative, as well as those reported in [39]. Despite this, they allow us to assess the effectiveness of the proposed method based on a widely accepted qualitative dynamical model thus representing the first attempt to model with a simple but efficient approach fundamental spatiotemporal dynamics linked to the occurrence of instable behavior in fusion plasma.

One of the negative consequences of plasma instabilities occurrences such as ELMs on nuclear fusion experiments is the damages

of plasma facing components (PFCs) and the consequent releases of materials inside plasma due to steep heat loads hitting PFCs. Thus, besides modeling plasma variables during the occurrences of instabilities in order to study effective control strategy, being able to monitor and predict heat loads on PFCs would be useful to deal with those.

In the next chapter, a model able to predict thermal loads on the PFCs adopted in FTU is identified and promising results presented.

Chapter 4

A SoS approach for Thermal Modeling Identification

In this chapter, the thermal model identification of the limiter surface placed in nuclear fusion plants facilities is presented. Experimental data measured at the Frascati TOKAMAK Upgrade (FTU) have been considered in order to identify a nonlinear dynamical model of the temperature distribution over the Cooled Lithium Limiter used in FTU. Three data-driven approaches have been followed: a linear autoregressive model, a nonlinear autoregressive model, and a Hammerstein model. The selection procedure of the relevant physical quantities will be outlined and a comparison among the obtained models will be given.

4.1 Introduction

The heat load on the PFCs installed in FTU, is evaluated by three different diagnostics: a fast infrared camera observing in real-time the whole limiter, a pair of thermocouples located on the limiter water circulation system and three Langmuir probes measuring the local electron temperature and density. From these source of data, information on the status of the temperature distribution over the limiter surface can be gained. However, models able to predict the dynamical behavior of temperatures can be of help in controlling the plasma behavior far from instabilities and disruptions, even in presence of uncertainties and sources of non ideal behavior. A dynamical model, in fact, would allow to predict the thermal behavior of the limiter surface, ensuring fundamental insights to define suitable realtime control strategies to maximize the performance of the limiter, i.e. to maintain the temperature over the whole limiter surface homogeneous, in order to address the power exhausts task.

In many works, the control strategies developed for the temperature regulation of the LLL surface exploit a physical model derived in [72]. It is an ideal approximation of the LLL thermal behavior and, although it can be very useful in standard working condition, it fails in modeling the system behavior in working conditions far from ideality, e.g. when disruptions occur.

In order to obtain an effective data-driven thermal model able to predict the global behavior during the experiments, this work aims to explore the performance of three different data-driven models, namely a linear autoregressive model (ARX), a nonlinear autoregressive model (NARX), and an Hammerstein model (HW) [73]. In order to do this, a

preliminary analysis of the available measured candidate input variables has to be performed with the aim of identifying those more related to the thermal process. This chapter is organized as follows: in Section 4.3 the input variables selection procedure is discussed, in Section 4.4 the linear and nonlinear models adopted are described, while Section 4.5 is devoted to the comparative analysis of models performance. Conclusive remarks on the suitability of the modeling approach are given in Section 4.6.

4.2 Data pre-processing

The dataset available from FTU diagnostics includes a large amount of measured and reconstructed variables related to the physical processes involved in a fusion experiments, i.e. electromagnetic, thermodynamic and geometrical quantities. Since we are interested in a dynamical model, we considered the dataset related to a specific experiment performed at FTU where disruption did not occur and in which the transient regime is significant. The variables in the dataset are measured over the entire duration $T = 1.734s$ of the selected pulse.

The main source of information for the identification procedure is the infrared (IR) camera located inside the TOKAMAK chamber. The IR camera is inserted through a port within the vacuum chamber wall and points to the limiter surface as schematically represented in Fig. 4.5. The output of the camera is a video stream taken with a frame rate of 120fps. The camera is pointed on the limiter surface whose shape can be clearly noticed in Figure 4.6 in which each pixel represents the temperature of a given area. The camera points also to

the areas surrounding the limiter (blue regions external to the limiter in Figure 4.6) which are neglected throughout this work. This is also the unique diagnostic able to spatially monitor the temperature over the limiter surface is the IR camera. In fact, a spatial information is fundamental to analyze how heat loads distribute over the adopted limiter surfaces. The IR camera needs a calibration phase able to correct the emissivity errors. Generally speaking, either the tabulated value of emissivity for the specific material of an object or a measurement of another diagnostic device is enough for the calibration phase when surface properties are homogeneous. In this case, a unique target temperature is considered for all the points of the object surface. When performing this procedure on liquid metal limiters in FTU, several practical aspects have to be taken into account.

In fact, as previously stated, a limiter based on an highly reactive liquid metal may undergo to spatio-temporal phenomena such as oxidation. Oxidation highly affect radiative properties of the object thus making the limiter surface heterogeneous. Since these kind of phenomena affect the measurement of the temperature, a punctual information of the temperature over the limiter surface is required. As a consequence, a further spatio-temporal diagnostic of the thermal distribution over the PFC surface should be used in order to calibrate point by point the images coming from the IR camera. In this section, a punctual correction map based on the fusion point detection of the liquid metal limiter installed in FTU is presented.

One of the temperature references that can be definitely verified is the temperature for which the material undergo a state phase transition such as the fusion point. Thus, by monitoring the thermal evolution of

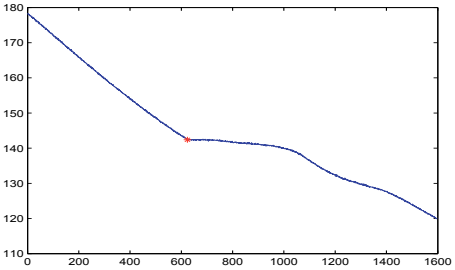

Fig. 4.1 Thermal evolution and corresponding melting point for the pixel (110,65) of the LLL recorded on the 07/13/2016.

the limiter during a phase transition, the fusion point can be detected and used as reference temperature for the calibration phase. This procedure can be applied to each pixel of the IR image measuring the temperature over the limiter surface. The cooling phase of the limiter has to be monitored and when the metal undergos a phase transition, an horizontal flat will characterize its temporal trend at the metal melting point. This point have to be recorded for each pixel and a first map of the fusion points as detected from the IR stream generated. From the direct comparison between the detected values and the reference tabulated temperature of the fusion point, a correction map can be built. It allows to monitor spatiotemporal phenomena occurring over the limiter surface and to correct thermal measurements point by point.

Thus, the first step is recording the thermal free evolution over the liquid metal limiter. It is shown in Fig. 4.1 where it is noticeable the flat line in corrispondence of the fusion point. Then, the reference fusion point temperature for both LLL and TLL are considered as 180.6 C° and 232 C° respectively. Results obtained for both the cases are shown

in Fig. 4.2 and 4.3 where it can be noticed how spatial phenomena can be caught by the spatial tool whose output show a continuous realistic thermal distribution especially for the LLL case. In fact, it was already expected that being lithium highly reactive, spatial phenomena occurred and thanks to this novel procedure, they can be deeply investigated. The cases analyzed for the LLL were the free evolution recorded at the end of each day taken from four consecutive experimental campaign. It is noteworthy the effectiveness of this approach to monitor the evolution of spatiotemporal phenomena, such as oxidation. From the first day to the fourth one, it can be noticed the evolution of the oxidation level due to the lithium reaction with oxygen.

For the TLL a more uniform map is obtained as it was expected. In fact, being low reactive, spatial phenomena are difficult to occur thus the correction map is almost uniform and equal to the tabulated emissivity value (0.4). In conclusion, the emergence of a spatial continuous map as a result of computing independent nodes action have shown the effectiveness of adopting an SoS approach in monitoring phenomena such as oxidation on LLL limiter paving the way for IR data correction.

A sample frame, taken when the plasma ring heats the limiter surface, as obtained from the camera after the pre-processing is reported in Figure 4.6. The inhomogeneous distribution is particularly relevant in some specific points, which have been recognized as hot spots strictly related to geometrical imperfections over the limiter [74].

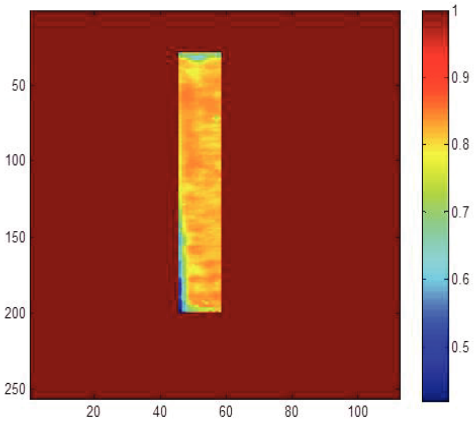

(a)

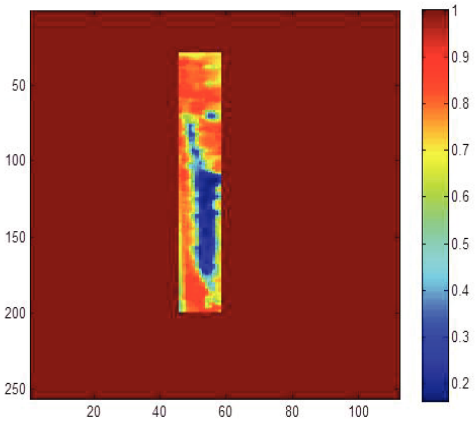

(b)

Fig. 4.2 Correction Map obtained from the correction tool by using IR frames recorded in July 12th and 13th 2016.

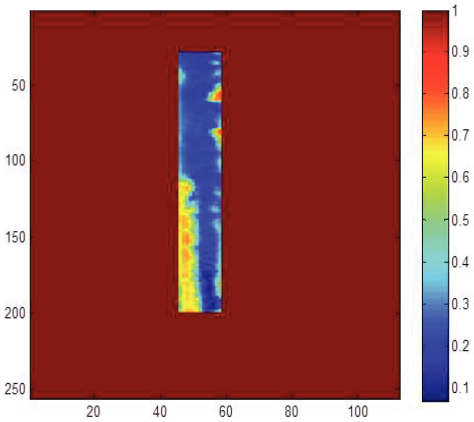

(a)

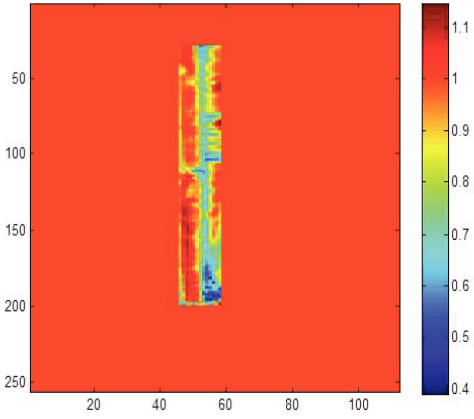

(b)

Fig. 4.3 Correction Map obtained from the correction tool by using IR frames recorded in July 14th and 15th 2016.

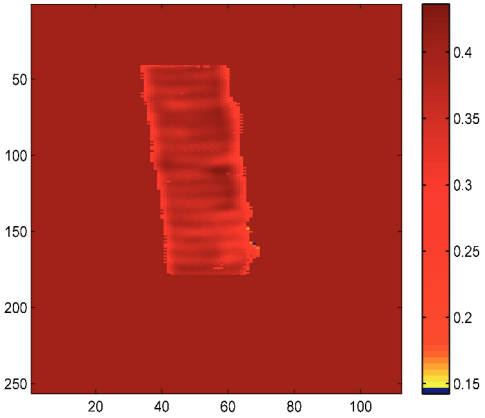

Fig. 4.4 TLL emissivity maps for TLL 11/11/16 experimental campaign.

4.3 Input variables selection

In order to perform the input variables selection procedure, we analyzed the correlation among the thermal information coming from each pixel of the IR camera with respect to each candidate variable. In particular, accordingly to the models discussed in [72, 75], we focused on the geometrical features of the plasma ring, including information on its shape and on its location within the TOKAMAK vacuum chamber. This choice is motivated by the fact that the main purpose of the proposed model is to provide useful information to control the shaping of the plasma so that a uniform temperature distribution can be attained over the limiter surface. Moreover, it is important to stress that geometrical properties of the plasma are determined on the basis of other character-

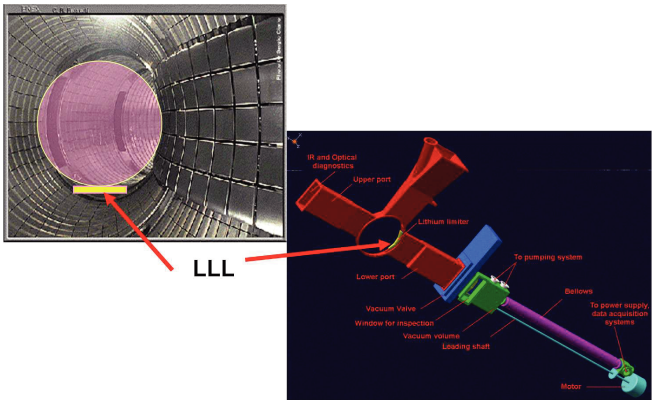

Fig. 4.5 Location of the LLL within the vacuum vessel and IR camera port.

istic measurements such as the plasma current I_{PL} and the toroidal field B_{TOR}.

The model is designed to identify the thermal process occurring over the limiter surface in response to heat load provided by the plasma. In particular, the heat transferred within the vacuum chamber to the LLL is represented by the subtraction between ohmic power and radiated power, which depends on the distance between the last closed magnetic surface and the limiter. In the discharges discussed in the contribution , in fact, the power provided by the additional heating system is negligible with respect to ohmic heating. Plasma current and vertical field both act on the plasma shaping and the corresponding geometrical features. Especially the ratio between the vertical and feedback field intensity determines the elongation and the radii of the plasma being the vertical field a function of the plasma current.

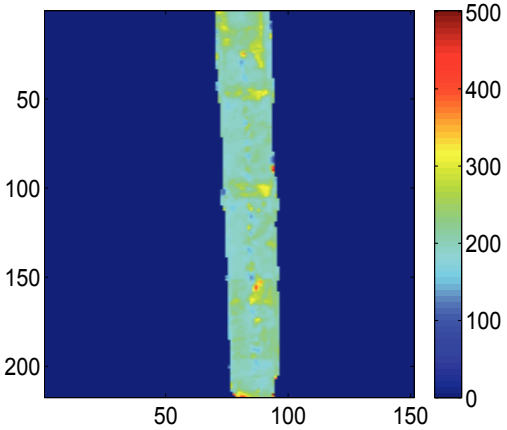

Fig. 4.6 Infrared camera output during an experiment. Temperatures are pre-processed to avoid camera systematic errors. Axes indicate pixels of the IR camera image.

Focusing on plasma geometrical properties, we can characterize 4 measures, the internal and external plasma radius, the upper and lower plasma radius from which it is possible to reconstruct the plasma elongation, i.e. the ratio between semi-axes, as schematically represented in Fig. 4.7.

The correlation analysis led to the results reported in Fig.4.8, where the cross-correlation between each plasma configuration parameter with respect to the temperature recorder over the whole extension of the limiter surface are reported. Each pixel of the figure represents the correlation coefficient, colorcoded according to the reported colorbar, between the transient regime of the temperature trend of the same pixel with respect to the trend of the given candidate variable. We report here

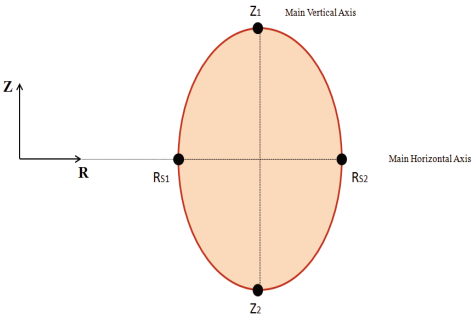

Fig. 4.7 Estimation of the geometrical features of the plasma ring: coordinates indicating the radii measures are taken by means of reconstruction based on magnetic measurements.

the results considering the elongation $E(k)$ and the upper radius $Z_1(k)$ for shot 377890. It is worth to notice that the shape of the limiter is clearly observable and the levels of correlation are higher than the 60% over the entire surface for both $Z1$ and E with a concentration on the rightmost part of the limiter due to the specific position of the plasma with respect to the limiter.

In order to further verify that the information provided by I_{PL} and B_{TOR} are already included in that provided by Z_1 and E, we computed the correlation coefficient also for these quantities. The correlation maps are reported in Fig. 4.9 and clearly indicate the same spatial distribution observed for Z_1 and E, but with lower correlation values.

The cross-correlation plots for Z_1 and E with respect to the temperature on a single pixel are reported as a function of the time-lags in Fig. 4.10. As it can be noticed, high correlation values are obtained also for larger time-lags.

The correlation analysis provides similar results for all pulses in the considered datasets. A number of other variables can been considered as potential inputs of the models, i.e. the internal and external plasma radii, since they appear highly correlated to the temperature over the limiter surface. However, due to the fact that the elongation of the plasma ring is evaluated also on the basis of these measurement, their influence of the model output did not provide a sensible increase in the performance.

Moreover, we focused on the fact that the temperature distribution can be driven also by a heat diffusion process occurring over the limiter surface. In order to catch this dynamics, we consider also the contribution given by temperatures of pixels located within a given distance. A schematic representation of the considered neighborhood is reported in Figure 4.11 where N_r represents the neighborhood radius with respect to pixel (i, j). Good results have been obtained with a neighborhood radius $N_r = 1$.

The following set of input variables has been therefore selected to model the temperature of pixel (i, j):

- $E(k)$: elongation of the plasma ring;
- $Z_1(k)$: upper radius of the plasma ring;
- $T_{i+N_i,j}(k), \ldots, T_{i+1,j}(k), T_{i-N_i,j}(k), \ldots, T_{i-1,j}(k)$, $T_{i,j+N_j}(k), \ldots, T_{i,j+1}(k), T_{i,j-N_j}(k), \ldots, T_{i,j-1}(k)$: temperature of the proximal pixels.

From a careful inspection of the available data in the time domain, five peculiar dynamical behaviors can been observed in different regions of the limiter surface, as shown in Fig. 4.12:

1. Initial peak: early onset of a temperature peak;
2. Fully saturated: temperature reaches the upper limit of the sensor range for the whole duration of the shot;
3. Partially saturated: temperature reaches the upper limit of the sensor range in a given time interval of the shot;
4. Disruption: temperature oscillates due to plasma disruption;
5. Normal: temperature increases towards a regime value and then collapse when plasma disappears.

The presence of an initial peak in the temporal trend of a pixel temperature is an hint of erroneous measurement of the actual temperature, it is probably due to modification of the light condition inside the TOKAMAK when the plasma lights up. The presence of saturations is strictly related to the hot spots areas [74] and indicates that the measured temperature reached the upper limit of the sensor range. The temperature behavior during a pulse whose outcome is a disruptive phenomenon sensibly differs from the normal behavior, since continuous oscillations can be observed until the plasma turns off. These four behaviors should not be considered in the model training, since they are not representative of the temperature dynamics in normal operative conditions, therefore they are not included in the training dataset. However, in order to test the models capabilities even in presence of nonideal behaviors, the temperatures recorded during disruptions are used in the validation dataset.

Since the magnitudes of the selected measurements are incomparable, the whole dataset has been normalized in the range $\left[\ -1; \quad 1 \ \right]$.

We have considered the FTU 2013 experimental campaign with the LLL, consisting in 26 complete pulses. The training set consists in 22 time-series for each pulse, each related to the trend of the temperature of a specific pixel of the video stream selected randomly in the set of the normal behavior pixels. Each time-series consists in 233 samples taken with a sampling time of $0.0085s$, for a grand total of 4860 training patterns for each pulse. The validation set is formed by 15 pixels for each pulse, including normal behaviors and disruptions, for a total of 3645 validation patterns for each pulse. Signals are taken randomly from all the 26 available pulses.

4.4 Model identification

In this work, we perform the comparison of three models, a linear and two nonlinear ones, identified by using the same identification dataset. Namely, we focused on a linear autoregressive model with exogenous inputs (ARX), a nonlinear ARX (NARX) implemented by using neural networks and an Hammerstein model (HM) [73].

We adopted the following regressors structure to estimate the output at time k:

$$
\begin{aligned}
&(T_{i,j}(k-n),\ldots,T_{i,j}(k-1),\\
&E(k-n_1),\ldots,E(k-1),\\
&Z_1(k-n_2),\ldots,Z_1(k-1),\\
&T_{i+N_i,j}(k-n_3),\ldots,T_{i+1,j}(k-1),\ldots,T_{i+1,j}(k-1),\\
&T_{i-1,j}(k-n_3),\ldots,T_{i-1,j}(k-1),\\
&T_{i,j+1}(k-n_3),\ldots,T_{i,j+1}(k-1),\\
&T_{i,j-1}(k-n_3),\ldots,T_{i,j-1}(k-1)),\\
&T_{i+1,j-1}(k-n_3),\ldots,T_{i+1,j-1}(k-1)),\\
&T_{i-1,j-1}(k-n_3),\ldots,T_{i-1,j-1}(k-1)),\\
&T_{i+1,j+1}(k-n_3),\ldots,T_{i+1,j+1}(k-1)),\\
&T_{i-,j+1}(k-n_3),\ldots,T_{i-,j+1}(k-1))
\end{aligned}
\tag{4.1}
$$

where $T_{i,j}(k)$ is the temperature of the $i,j-th$ pixel at time k, $E(k)$ is the elongation of the plasma ring at time k, $Z_1(k)$ is the upper radius of the plasma ring at time k. The number of regressors is defined by n (regressors of the state), n_1 (regressors of the elongation), n_2 (regressors of the internal radius), and n_3 (regressors of the proximal temperatures).

The number of regressors for each variable has been selected for each model by using a trial-and-error procedure evaluating a number of performance indices such as the correlation coefficient between estimated and measured output, the root mean square error (RMS), the maximum of the absolute value of the error (MAE). In the following, we give details on the performance of the best models for each of the three classes considered.

4.4.1 ARX linear model

Among the linear autoregressive model considered in the trial-and-error procedure, we present here results related to the best performance corresponding to a model with $n = 3$ poles, and two zeros, i.e. $n_1 = n_2 = n_3 = 2$.

The identification of the ARX model leads to the estimation of the coefficients of the following polynomial:

$$
\begin{aligned}
&T_{i,j}(k) = 0.8536T_{i,j}(k-1) + 0.1785T_{i,j}(k-2) \\
&-0.0831T_{i,j}(k-3) + 0.01184T_{i-1,j-1}(k-1) \\
&-0.03215T_{i-1,j-1}(k-2) + 0.04667T_{i,j-1}(k-1) \\
&-0.02897T_{i,j-1}(k-2) + 0.02028T_{i+1,j-1}(k-1) \\
&-0.01781T_{i+1,j-1}(k-2) + 0.1103T_{i-1,j}(k-1) \\
&-0.06416T_{i-1,j}(k-2) - 0.08168T_{i+1,j}(k-1) \\
&+0.07613T_{i+1,j}(k-2) + 0.1581T_{i-1,j+1}(k-1) \\
&-0.1743T_{i-1,j+1}(k-2) + 0.01438T_{i,j+1}(k-1) \\
&+0.01556T_{i,j+1}(k-2) - 0.08213T_{i+1,j+1}(k-1) \\
&+0.06798T_{i+1,j+1}(k-2) - 0.08E(k-1) \\
&+0.06419E(k-2) + 0.09457Z_1(k-1) - 0.06456Z_1(k-2)
\end{aligned}
\tag{4.2}
$$

The model results, after denormalization of the model outputs, reported in Figure 4.13 are related to a pixel belonging to the validation set. The trend of the temperature obtained as output of the identified model and the corresponding measured temperature are show in Figure 4.13(a). The autocorrelation of the error (Fig. 4.13(b)), the distribution of the residuals (Fig. 4.13(c)) and the normal probability

plot (Fig. 4.13(d)) are also reported. Similar results have been obtained for all the pixel belonging to the validation set.

As it can be observed from Figures 4.13, the ARX model performance are satisfactory. The overall performance indices are evaluated in the following section.

4.4.2 NARX nonlinear model

As a second approach a nonlinear model has been identified. The NARX model, in fact, allows to consider nonlinear effects neglected by the ARX identification. Using the regressors structure (4.1), the NARX model has been implemented by using multilayer perceptron (MLP) neural networks [76–78]. The use of neural networks in modeling plasma behavior has already proven to be effective [79–82]. Best performance has been obtained with a single hidden layer MLP with 8 neurons. We present here results related to the best performance corresponding to a model with $n = 3$, and $n_1 = n_2 = n_3 = 2$.

The performance of the identified NARX model are shown in Figure 4.14, after denormalization of the model outputs. The temperature obtained as output of the model for a single pixel of the validation set is shown in Figure 4.14(a) together with the corresponding measured temperature. The three plots reported in Figures 4.14(b), 4.14(c), and 4.14(d) show the residuals autocorrelation, histogram, and normal probability plot. Better results with respect to the ARX model are obtained considering also the other pixels of the validation set.

4.4.3 Hammerstein model

Taking into account that the behavioral model reported in [72] encompasses a single static nonlinearity applied to the geometrical features of the plasma ring, we decided to identify an Hammerstein model. Despite this, our model sensibly differs from that discussed in [72] where the distance with respect to the limiter surface is approximated, since calculating the exact distance would require to solve a fourth-order polynomial and a nontrivial trigonometric equation. Our approach is not physics-based and therefore it is able to estimate both parameters and functional relationship between plasma geometrical features and temperature distribution over the entire limiter surface maintaining a mathematical structure which is physics-relevant.

The Hammerstein structure is schematically represented in Figure 4.15. In its most general form, it describes the system dynamics by using a single static nonlinear block in series with a dynamic linear block. The input signal $u(k)$ passes through the nonlinear block $f(\cdot)$ and then through the dynamic linear block to produce the output signal. Best results have been obtained with a linear block with $n = 3$ poles, $n_1 = n_2 = n_3 = 1$ zero, while the input nonlinearities are identified using neural networks with three units applied to both the elongation $E(k)$ and the upper radius $Z_1(k)$. Temperatures are not subjected to a nonlinear function.

The input/output relationship of the Hammerstein model is:

$$
\begin{aligned}
T_{i,j}(k) &= \tfrac{B_1(z)}{F_1(z)} T_{i-1,j-1}(k) + \tfrac{B_2(z)}{F_2(z)} T_{i,j-1}(k) \\
&+ \tfrac{B_3(z)}{F_3(z)} T_{i+1,j-1}(k) + \tfrac{B_4(z)}{F_4(z)} T_{i-1,j}(k) \\
&+ \tfrac{B_5(z)}{F_5(z)} T_{i,j+1}(k) + \tfrac{B_6(z)}{F_6(z)} T_{i-1,j+1}(k) \\
&+ \tfrac{B_7(z)}{F_7(z)} T_{i,j+1}(k) + \tfrac{B_8(z)}{F_8(z)} T_{i+1,j+1}(k) \\
&+ \tfrac{B_9(z)}{F_9(z)} f_1(E(k)) + \tfrac{B_{10}(z)}{F_{10}(z)} f_2(Z_1(k))
\end{aligned}
\tag{4.3}
$$

where f_1 and f_2 are the nonlinear functions identified for the two input variables $E(k)$ and $Z_1(k)$ as reported in Fig. 4.16, while the polynomials $B(z)$ and $F(z)$ are reported in Tab. 4.1 for each input variable.

The four plots reported in Figure 4.17 show the performance of the Hammerstein model identified by means of an output error minimization performed using a subspace Gauss-Newton least square algorithm [73] and a subsequent refinement based on a prediction-error minimization algorithm.

The temperature predicted by the model is shown in Figure 4.17(a) together with the corresponding measured temperature. The three plots reported in Figures 4.17(b), 4.17(c), and 4.17(d) show the residuals autocorrelation, histogram, and normal probability plot.

As it can be observed from Figures 4.17, the model performance are sensibly higher with respect to both the ARX and NARX identification. This will be remarked in the following section by means of the reported overall performance indices.

4.5 Comparative analysis

In this section the three models identified have been evaluated and compared by means of a number of performance indices. The values

of the correlation coefficient (CC) between estimated and measured output, the root mean square error (RMS), and the maximum of the absolute value of the error (MAE) are reported for the identification set in Table 4.2, and for the validation set in Table 4.3.

In order to directly compare the capabilities of the three models, we report in Figure 4.18 the trends of the output of the models for four further pixels of the test set, together with the actual measured temperature. The identification of a linear model provides a simple and reliable tool but at the cost of neglecting nonlinear dynamics which may be fundamental in reconstructing the thermal behavior. The ARX model, in fact, is able to predict the trend of the real data, even if the reconstructed values are slightly different. The use of the nonlinear model NARX leads to an increasing in the model performance, despite a corresponding increase in the model complexity and a difficult physical interpretation of its parameters.
The adoption of a model which links the simple structure of linear models with the nonlinear features introduced by input functions allows to improve the model performance with a slight increase in its complexity.

On the basis of the time plots and of the performance indices evaluated in this section, the Hammerstein model provides a better identification of the thermal behavior of the limiter surface. This confirms the theoretical expectations of the model reported in [72], and being identified from experimental data, introduces a sensible improvement in modeling the transient regime. Furthermore, while the theoretical model does not take into account the spatial coordinates of the limiter surface, our model encompasses this aspect.

The good performance of the Hammerstein model are particularly relevant when predicting abnormal behavior occurring during disruptions. In Fig. 4.19 the temporal behavior of the temperature of a single pixel over the limiter during a shot in which the plasma current is intentionally set to a lower value is reported and compared with the predicted output provided by the three models. The peculiar behavior of this experiment is due to a non optimal control of the plasma ring position. Nonetheless, the model is still able to accurately predict the thermal behavior. The superiority of the Hammerstein model prediction is, hence, evident.

4.6 Conclusion

The possibility to derive a dynamical data-driven model of the temperature distribution over the limiter surface in TOKAMAKs is a fundamental milestone in the view of controlling the plasma experiment far from disruptive events. In this chapter, we report the result of three different models which allow us to estimate the temporal evolution of the temperature spatial distribution on the limiter surface operating at the FTU. The models take into account both the effects of a set of external variables, such as those related to the geometrical features of the plasma ring, and the effects of the temperatures of neighboring regions in order to cope with the heat diffusion process occurring over the surface. The models reported in this chapter pave the way to the definition of new and more accurate strategies to control the plasma ring in order to avoid disruptions.

Three different models have been identified by using a suitable set of experimental measurements, namely a linear autoregressive model, a nonlinear autoregressive model, and an Hammerstein model. The analysis of models performance leads to assess the suitability of the three approaches which produce good results. However, the Hammerstein model, which reveals to be more adherent to the theoretical background of the physical process, shows better statistical properties of the error dynamics along with a relatively simple structure in which only static input nonlinearities are considered. Furthermore, the Hammerstein model is able to predict temperature behavior also in presence of abnormal plasma experiments, i.e. those experiments in which the plasma ring shows instabilities leading to an early end.

The proposed model can be embedded in real-time monitoring systems, such that currently running at JET [83] in which a physics-based model similar to that proposed in [72] is implemented.

In the view of the application in a ITER-like scenario, in which diverted plasmas will be considered and where the power generated by the additional heating systems is not negligible, it must be pointed out that the experimental conditions considered in our work imply that the power is concentrated on a surface of $50cm^2$, leading to heat loads in the order of $10MW/m^2$, which are consistent to the reference adopted as maximum heat loads for ITER. Besides this consideration, the proposed modeling approach includes the parameter N_r, which we fixed as $N_r = 1$. Increasing N_r allows to tackle diffusion processes acting on different spatial and temporal scales, thus it can be fixed accordingly to the specific case study, allowing the adoption of the proposed modeling approach in different scenarios.

Finally, the proposed modeling approach is able to provide reliable performance even in the case of pulse durations lower than that planned for ITER, making FTU a valid benchmark, especially in the view of a real-time control of plasma shaping.

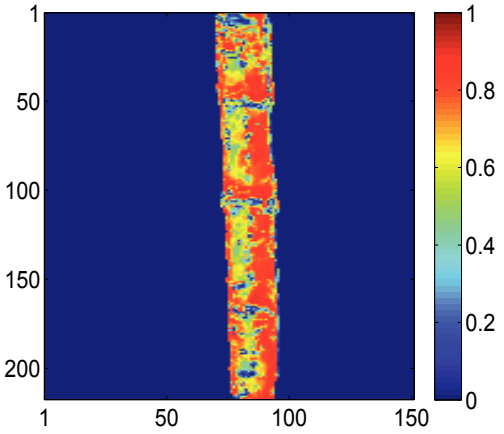

(a)

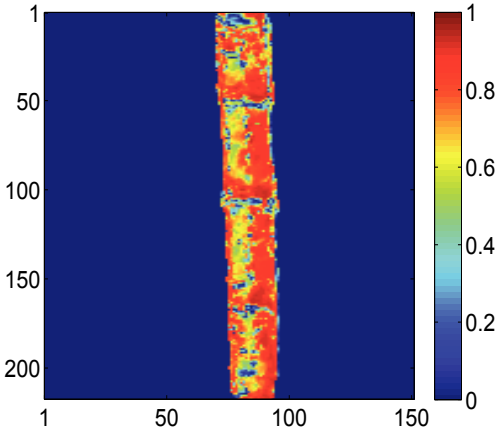

(b)

Fig. 4.8 Correlation analysis between plasma ring elongation (a) and upper radius (b) with respect to temperatures over the limiter surface. The values of the correlation coefficient are colorcoded according to the colorbar: the temperatures measured by the camera are highly correlated with the plasma ring elongation over the entire surface. Axes indicate pixels of the IR camera image.

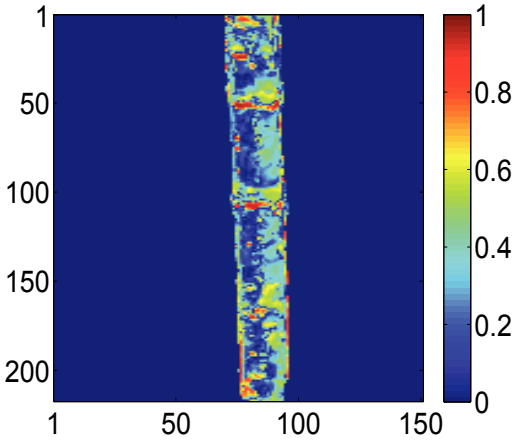

(a)

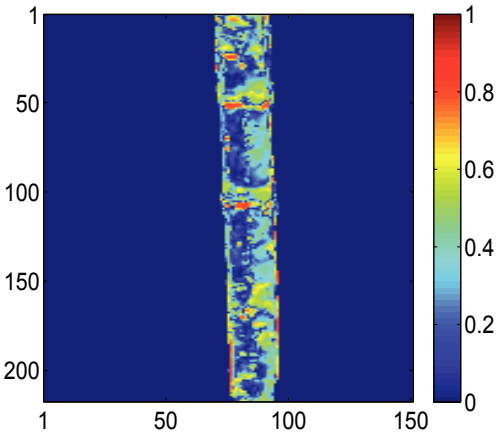

(b)

Fig. 4.9 Correlation analysis between (a) toroidal field and (b) plasma current with respect to temperatures over the limiter surface. The values of the correlation coefficient are colorcoded according to the colorbar: the temperatures measured by the camera are highly correlated with the plasma ring elongation over the entire surface. Axes indicate pixels of the IR camera image.

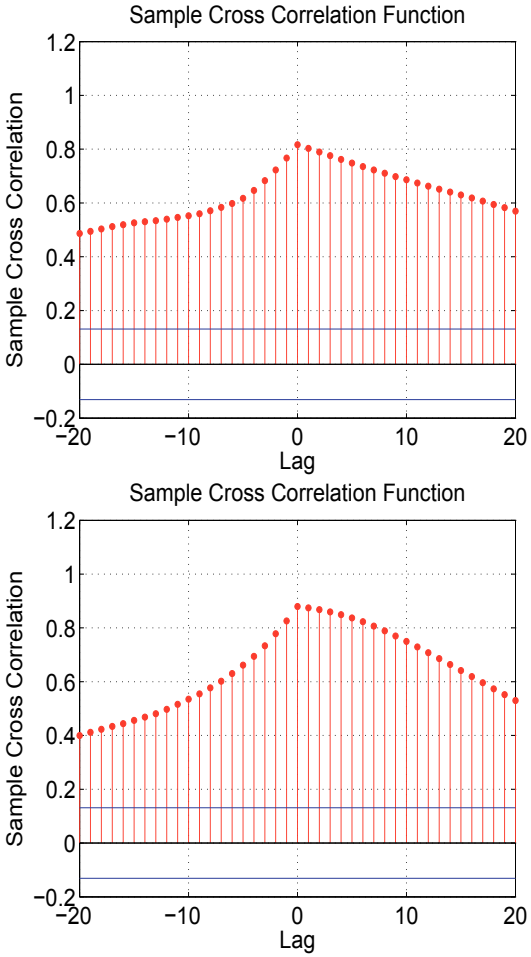

Fig. 4.10 Plot showing the correlation coefficient as a function of the lag between a specific pixel of the IR camera and each geometrical plasma variables.

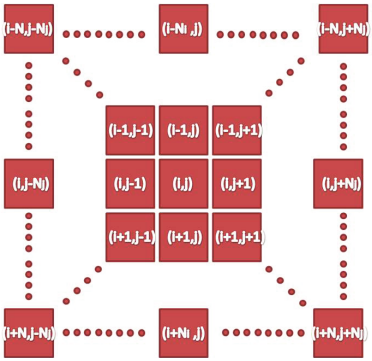

Fig. 4.11 Schematic representation of the interaction radius between pixel considered to take into account the heat diffusion process acting over the limiter surface.

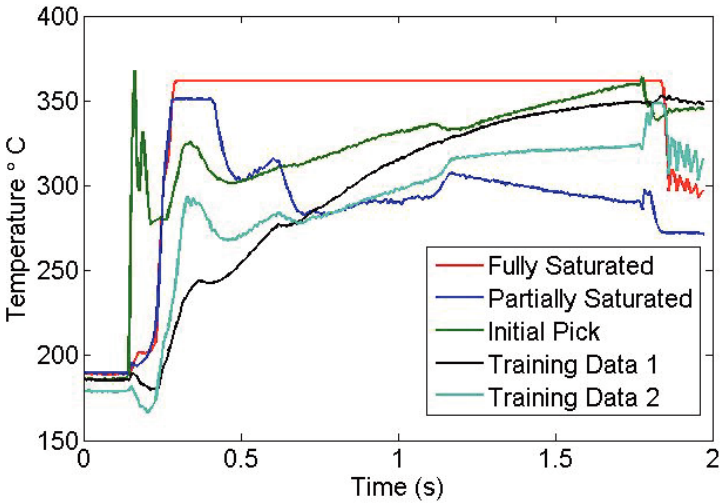

Fig. 4.12 Signals prototypes that have been neglected from the training dataset.

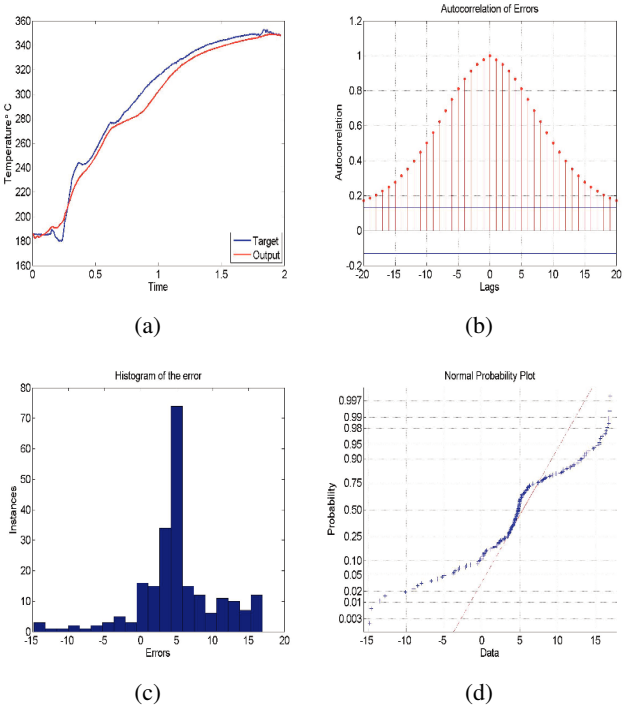

Fig. 4.13 Performance of the ARX model evaluated for one pixel of the validation set: trends of the measured and modeled temperature (a), error autocorrelation (b), error histogram (c), and error normal plot (d).

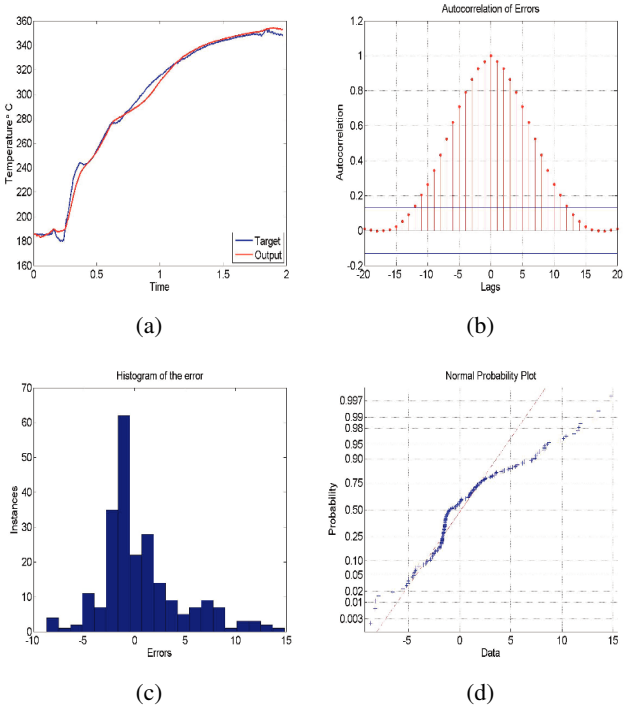

Fig. 4.14 Performance of the NARX model evaluated for one pixel of the validation set: trends of the measured and modeled temperature (a), error autocorrelation (b), error histogram (c), and error normal plot (d).

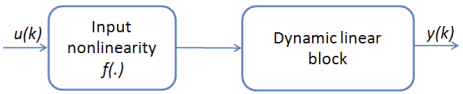

Fig. 4.15 Block diagram of the considered Hammerstein model.

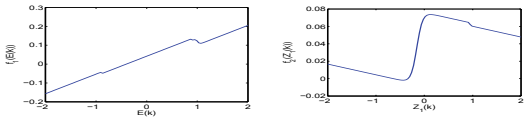

Fig. 4.16 Input nonlinearities identified for the Hammerstein model: (a) elongation, and (b) upper radius.

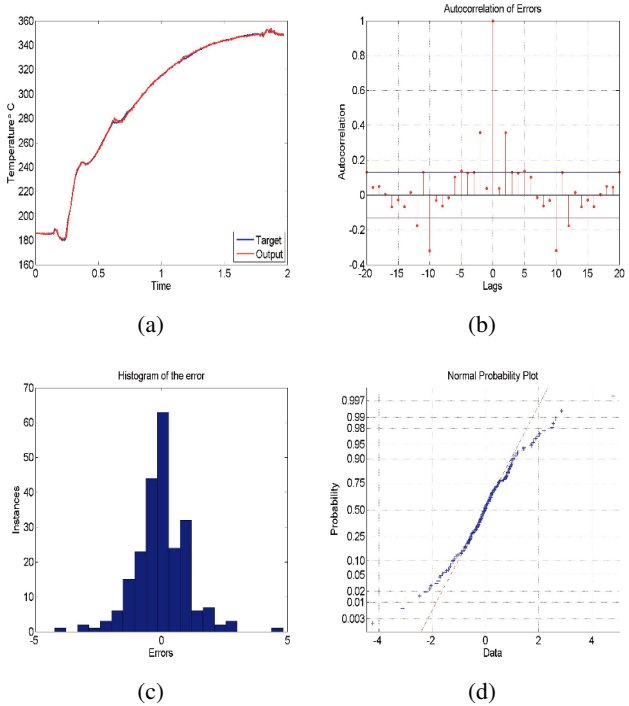

(a) (b)

(c) (d)

Fig. 4.17 Performance of the Hammerstein model evaluated for one pixel of the validation set: trends of the measured and modeled temperature (a), error autocorrelation (b), error histogram (c), and error normal plot (d).

Table 4.1 Transfer functions identified for the Hammerstein model.

Input	$\frac{B(z)}{F(z)}$
$T_{i-1,j-1}(k)$	$\frac{-0.115z^{-1}-0.2439z^{-2}}{1+0.07z^{-1}-0.2314z^{-2}+0.2534z^{-3}}$
$T_{i,j-1}(k)$	$\frac{0.7z^{-1}-0.7z^{-2}}{1-0.817z^{-1}-0.3579z^{-2}+0.175z^{-3}}$
$T_{i+1,j-1}(k)$	$\frac{-0.0824z^{-1}0.0497z^{-2}}{1-0.9157z^{-1}-0.7545z^{-2}+0.08327z^{-3}}$
$T_{i-1,j}(k)$	$\frac{0.4146z^{-1}-0.3758z^{-2}}{1-1.3157z^{-1}+0.4068z^{-2}-0.0064z^{-3}}$
$T_{i+1,j}(k)$	$\frac{0.1408z^{-1}-0.1236z^{-2}}{1-1.2301z^{-1}-0.0591z^{-2}+0.3623z^{-3}}$
$T_{i-1,j+1}(k)$	$\frac{0.0062z^{-1}-0.0012z^{-2}}{1+0.7747z^{-1}-0.7867z^{-2}-0.89z^{-3}}$
$T_{i,j+1}(k)$	$\frac{0.2551z^{-1}-0.019z^{-2}}{1+0.2636z^{-1}-0.1207z^{-2}+0.2791z^{-3}}$
$T_{i+1,j+1}(k)$	$\frac{-0.0284z^{-1}+0.0264z^{-2}}{1-0.9336z^{-1}-0.8531z^{-2}+0.8283z^{-3}}$
$E(k)$	$\frac{-0.3z^{-1}+z^{-2}}{1+0.2415z^{-1}-0.7681z^{-2}-0.3223z^{-3}}$
$Z_1(k)$	$\frac{-1.6587z^{-1}+z^{-2}}{1-0.7333z^{-1}-0.9441z^{-2}-0.7146z^{-3}}$

Table 4.2 Performance indices for the training phase.

	CC	*RMS*	*MAE*
ARX	0.981	5.624	19.056
NLARX	0.989	4.265	18.418
HM	0.996	1.926	12.6

Table 4.3 Performance indices for the validation phase.

	CC	*RMS*	*MAE*
ARX	0.972	8.3	23.5
NLARX	0.983	6.8	22.7
HM	0.995	2.6	16.3

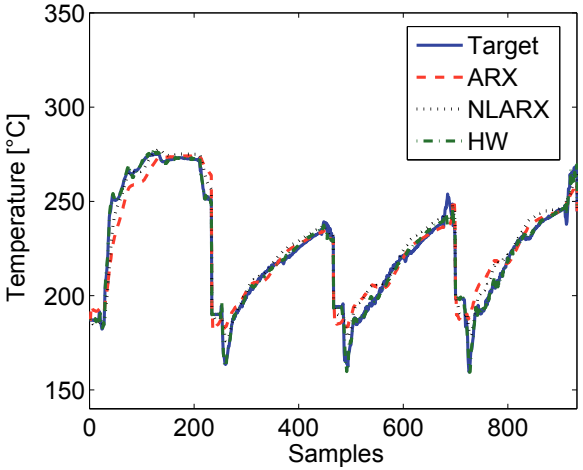

Fig. 4.18 Temporal evolution of the temperature of four non contiguous pixels from the test dataset. Trends are concatenated. Comparison between the output of the three models with respect to the measured variable.

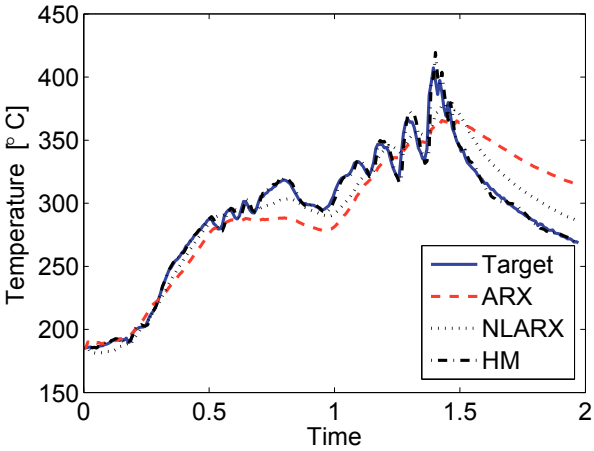

Fig. 4.19 Temporal evolution of the temperature of a pixel during a disruption: comparison between the output of the three models with respect to the measured variable.

Chapter 5

Conclusion

In this work, a SoS approach has been used in order to improve the performance of nuclear fusion machines. Each facet has been developed by integrating the actions of single units being able to elicit an SoS emerging behaviour. In particular, suitably controlling the relevant parameters, each SoS has been driven to the desired state. As shown by the obtained results, the performance of the TOKAMAK machines by using the adopted SoS strategies can be widely improved. Plasma instabilities leading to steep heat loads hitting the plasma-facing component, and consequently leading to plasma disruptions, may be opportunely modeled and an suitable control strategy designed. The thermal loads over the CLL limiter investigated as plasma-facing components has been modeled being able to spatially predict the thermal distribution over its surface thus being able to control heat loads leading again to disruptive events. Thus, as overall result, a step forward plasma disruptions avoidance has been performed by both opportunely modeling plasma instabilities and by predicting the thermal behaviour of

the plasma-facing components therefore being able to act before the disruptive events occur.

Bibliography

[1] Popper, S. W., Bankes, S. C., Callaway, R., DeLaurentis, D. (2004). System of systems symposium: Report on a summer conversation. Potomac Institute for Policy Studies, Arlington, VA, 320.

[2] ISO/IEC/IEEE “Systems and software engineering – System life cycle processes,” in ISO/IEC/IEEE FDIS P15288:2015 , vol., no., pp.1-122, May 15 2015

[3] Terry Bahill,"A Consensus of the INCOSE Fellows", *INCOSE*, 2006.

[4] C. Carnevale ; G. Finzi ; E. Pisoni ; M. Volta," A system of systems for air quality decision making", *Incose2012 7th International Conference on System of Systems Engineering (SoSE)*, 258 - 263,2012.

[5] De Laurentis, D., "Understanding Transportation as a System of Systems Problem." *System of Systems Engineering: Innovations for the 21st Century*, M. Jamshidi, ed., Wiley, 520-541 (2009).

[6] A. Morkevicius, L. Bisikirskiene, and G. Bleakley, "Using a systems of systems modeling approach for developing Industrial In-

ternet of Things applications", *System of Systems Engineering Conference (SoSE)*, 2017 12th (pp. 1-6). IEEE.(2017)

[7] Schuck, T. M., and Kilian, J. C. (2017, June). Trends in large scale systems-of-systems for multi-national missile defense. In System of Systems Engineering Conference (SoSE), 2017 12th (pp. 1-6). IEEE.

[8] A. Ferrara,A. N. Oleari, S. Sacone, and S. Siri. "Freeways as systems of systems: A distributed model predictive control scheme", *IEEE Systems Journal*, 9(1), 312-323,(2015)

[9] Giammarco, K. (2017, June). Practical modeling concepts for engineering emergence in systems of systems. In System of Systems Engineering Conference (SoSE), 2017 12th (pp. 1-6). IEEE.

[10] F. Romanelli, *Overview of the JET results*, Nuclear Fusion, **55**(10), 104001, 2015.

[11] L. C. Woods, *Theory of TOKAMAK transport. New aspects for nuclear fusion reactor design*, Wiley VCH Verlag, Weinheim, 2006

[12] M. Kikuchi, K. Lackner, Minh Quang Tran, *Fusion Physics*, 2012

[13] Marco Ariola, Alfredo Pironti, *Magnetic Control of TOKAMAK Plasmas*

[14] Associazione EURATOM-ENEA sulla Fusione, Centro Ricerche Frascati, *The Frascati TOKAMAK Upgrade (FTU) after Four Years of Operation*,

[15] Vega,et al. Results of the JET real-time disruption predictor in the ITER-like wall campaigns. *Fusion Engineering and Design*, 88(6-8), 1228-1231,(2013). doi:101016/jfusengdes201303003.

[16] G.Mazzitelli, *Presentation of FTU at University of Catania*, 2012

[17] http://jolisfukyu.tokai-sc.jaea.go.jp/fukyu/mirai-en/2006/3_12.html

[18] Plasma instabilities. (n.d.). Retrieved November 25, 2017, from https://www.euro-fusion.org/fusion/spot-on-jet-operations/maintaining-the-plasma/plasma-instabilities/

[19] Haines, M. G., " An analytic model of radiative collapse of a Z-pinch". *Plasma Physics and Controlled Fusion*, 31(5), 759, 1989.

[20] Zagorski, R., and Gerhauser, H., " Numerical Modelling of Marfe Phenomena in TEXTOR Tokamak". *Physica Scripta*, 70(2-3), 173, 2004.

[21] Pankin, A. Y., Rafiq, T., Kritz, A. H., Park, G. Y., Chang, C. S., Brunner, D., and Ku, S., "Kinetic modeling of divertor heat load fluxes in the Alcator C-Mod and DIII-D tokamaks". *Physics of Plasmas*, 22(9), 092511, 2015.

[22] Rasmussen, J. J., Nielsen, A. H., Madsen, J., Naulin, V., and Xu, G. S.,. "Numerical modeling of the transition from low to high confinement in magnetically confined plasma". *Plasma Physics and Controlled Fusion*, 58(1), 014031, 2015.

[23] D Kalupin, M Z Tokar, P Dumortier, A Messiaen, D Reiser, S Soldatov, B Unterberg, G van Wassenhove and R Weynants, "

Modelling of confinement degradation in the radiative improved mode caused by a strong gas puff", *Plasma Phys. Control. Fusion*, 43 (2001) 945-957

[24] A. Bondeson, R.D. Parker, M. Hugon and P. Smeulders, "MHD modelling of density limit disruptions in tokamaks", *Nuclear Fusion*, Volume 31, 1991.

[25] S Tholerus, T Hellsten and T Johnson, " Modeling the dynamics of toroidal Alfven eigenmodes", *13th IAEA Technical Meeting on Energetic Particles in Magnetic Confinement Systems*, Beijing, China, September 17 - 20, 2013

[26] Hannan, A.. "Modelling Ion Cyclotron Resonance Heating and Fast Wave Current Drive in Tokamaks", *(Doctoral dissertation, KTH Royal Institute of Technology)*, 2013.

[27] Goloborod'ko, V. Y., Belikov, V. S., Reznik, S. N., and Yavorskij, V. A., "Modeling of core-localized Alpha-Driven Alfven Eigenmodes in TFTR", *IAEA 2012*.

[28] B Coppi, F. Porcelli, *Theoretical Model of Fishbone Oscillations in Magnetically Confined Plasma*.

[29] S. Strogatz, *Nonlinear Dynamics And Chaos: With Applications To Physics, Biology, Chemistry, And Engineering*, Westview Press, 2001.

[30] F. C. Moon, *Chaotic Vibrations*, Wiley, 2004.

[31] A. Buscarino, L. Fortuna, M. Frasca and G. Sciuto, *A Concise Guide to Chaotic Electronic Circuits*, SpringerBriefs, 2014.

[32] W. Arter, Symmetry Constraints on the Dynamics of Magnetically Confined Plasma, *Physical Review letters*, 102(19), 195004, 2009.

[33] B. Gilbert, A Precise Four-Quadrant Multiplier with Subnanosecond Response, *IEEE Journal of Solid-State Circuits*, 3(4), 365-373, 1968.

[34] G. Manganaro and J. Pineda de Gyvez, A Four-Quadrant S^2I Switched-Current Multiplier, *IEEE Transactions on Circuits and Systems – I I: Analog and Digital Signal Processing*, 45(7), 791-799, 1998.

[35] A. Baranyi and L. O. Chua, Dynamic model for the analog multiplier, *IEEE Transactions on Circuits and Systems*, 29(2), 65-76, 1982.

[36] A. Wolf, J. B. Swift, H. L. Swinney and J. A. Vastano, Determining Lyapunov exponents from a time series, *Physica D: Nonlinear Phenomena*, 16(3), 285-317, 1985.

[37] M. Schmidt, H. Lipson, Distilling Free-Form Natural Laws from Experimental Data, *Science*, 324(5923), 81–85, 2009.

[38] G.T.A. Huysmans, O. Czarny, *MHD stability in X-point geometry: simulation of ELMs*, Nuclear Fusion, **47**(7), 659, 2007.

[39] D. Constantinescu, O. Dumbrajs, V. Igochine, K. Lackner, R. Meyer-Spasche, H. A. U. T. Zohm, *A low-dimensional model system for quasi-periodic plasma perturbations*, Physics of Plasmas **18**(6), 062307,2011.

[40] Arduino board, https://www.arduino.cc/.

[41] Arturo Buscarino, Luigi Fortuna, Mattia Frasca, *Essentials of Nonlinear Circuit Dynamics with MATLAB and Laboratory Experiments*, April 21, 2017 by CRC Press.

[42] Constantinescu, D., Dumbrajs, O., Igochine, V., Lackner, K., Zohm, H., and Team, A. U. (2013). RMP ELM suppression analysis by means of a low-dimensional model system for quasi-periodic plasma perturbations. In 40th EPS Conference on Plasma Physics. European Physical Society.

[43] Evans, T. E., Moyer, R. A., Burrell, K. H., Fenstermacher, M. E., Joseph, I., Leonard, A. W. et al. (2006). Edge stability and transport control with resonant magnetic perturbations in collisionless tokamak plasmas. nature physics, 2(6), 419-423.

[44] A. Turing, "The chemical basis of morphogenesis", *Philosophical Transactions of the Royal Society of London B: Biological Sciences*, **237**, pp. 37-72, 1952.

[45] A. K. Harris, D. Stopak, and P. Warner, "Generation of spatially periodic patterns by a mechanical instability: a mechanical alternative to the Turing model", *Development*, **80**(1), pp. 1-20, 1984.

[46] L. Goras, and L. O. Chua, "Turing patterns in CNNs. II. Equations and behaviors", *IEEE Transactions on Circuits and Systems I: Fundamental Theory and Applications*, **42**(10), pp. 612-626, 1995.

[47] U. Daybelge, C. Yarim, and A. Nicolai, “Spatiotemporal oscillations in TOKAMAK edge layer and their generation by various mechanisms”, 24th IAEA Fusion Energy Conf., 2012.

[48] G. Manganaro, P. Arena, and L. Fortuna, *Cellular Neural Networks: Chaos, Complexity and VLSI Processing. Vol. 1.*, Springer Science & Business Media, 1999.

[49] V. K. Vanag, and I. R. Epstein, ”Cross - diffusion and pattern formation in reaction - diffusion systems”, *Physical Chemistry Chemical Physics*, **11**(6), pp. 897-912, 2009.

[50] D. B. Strukov, G. S. Snider, D. R. Stewart, and R. Stanley Williams, “The missing memristor found”, *Nature* **453**, pp. 80-83, 2008.

[51] M. Itoh, and L. O. Chua, “Memristor oscillators”, *International Journal of Bifurcation and Chaos*, **18**(11), pp. 3183-3206, 2008.

[52] L. Chua, “Everything you wish to know about memristors but are afraid to ask,” *Radioengineering*, 24(2), 319, 2015.

[53] Y. V. Pershin, M. Di Ventra, “Practical approach to programmable analog circuits with memristors,” *IEEE Transactions on Circuits and Systems I: Regular Papers* **57**(8), pp. 1857-1864, 2010.

[54] R. Tetzlaff, *Memristors and Memristive Systems*, New York: Springer, 2014.

[55] D. Yu, H. H. C. Iu, Y. Liang, T. Fernando, L. O. Chua, “Dynamic Behavior of Coupled Memristor Circuits,” *IEEE Transactions on Circuits and Systems I: Regular Papers* **62**(6), pp. 1607-1616, 2015.

[56] A. Ascoli, S. Slesazeck, H. Mahne, R. Tetzlaff, T. Mikolajick, "Nonlinear dynamics of a locally-active memristor," *IEEE Transactions on Circuits and Systems I: Regular Papers* **62**(4), pp. 1165-1174, 2015.

[57] L. O. Chua, "Memristor-the missing circuit element", *IEEE Trans. Circuit Theory*, **18**(5), pp. 507-519, 1971.

[58] A. Buscarino, L. Fortuna, M. Frasca, and L. V. Gambuzza, "A chaotic circuit based on Hewlett-Packard memristor", *Chaos: An Interdisciplinary Journal of Nonlinear Science*, **22**(2), 2012.

[59] A. Buscarino, L. Fortuna, M. Frasca, and L. V. Gambuzza, "A gallery of chaotic oscillators based on HP memristor", *International Journal of Bifurcation and Chaos*, **23**(5), 2013.

[60] V. T. Pham, A. Buscarino, L. Fortuna, and M. "Autowaves in memristive cellular neural networks", *International Journal of Bifurcation and Chaos*, **22**(8), 1230027, 2012.

[61] J. D. Murray, *Mathematical Biology. II Spatial Models and Biomedical Applications*, Springer-Verlag New York Incorporated, 2001.

[62] A. Buscarino, C. Corradino, L. Fortuna, M. Frasca , L.O. Chua, *Turing Patterns in Memristive Cellular Nonlinear Networks*, IEEE Transactions on Circuits and Systems I: Regular Papers, **63**(8), 1222-1230. 2016.

[63] Q. Ouyang, R. Li, and H.L. Swinney, "Dependence of Turing pattern wavelength on diffusion rate", *The Journal of chemical physics*, **102**(6), pp. 2551-2555, 1995.

[64] H. Shoji, K. Yamada, D. Ueyama, T. Ohta, "Turing patterns in three dimensions," *Physical Review E*, **75**, pp. 046212-1-13, 2007.

[65] J. Wesson, *TOKAMAKs*, Clarendon Press, Oxford, 2004.

[66] ASDEX Team, *The H-mode of ASDEX*, Nuclear Fusion **29**(11) 1959, 1989.

[67] D. Constantinescu, O. Dumbrajs, V. Igochine, K. Lackner, H. Zohm, *Bifurcations and fast-slow dynamics in a low dimensional model for quasi-periodic plasma perturbations*, Romanian Reports in Physiscs **67**(3), 1049-1060 ,2015.

[68] A. Kirk, N.B. Ayed, G. Counsell, B. Dudson, T. Eich, A. Herrmann, B. Koch, R. Martin, A. Meakins, S. Saarelma, R. Scannell, S. Tallents, M. Walsh, H.R. Wilson, and the MAST Team, *Filament structures at the plasma edge on MAST*, Plasma physics and controlled fusion, **48**(12B), B433, 2006.

[69] K. Kovarik, I. Duran, J. Stöckel, J. Adamek, M. Spolaore, N. Vianello, *Properties of filamentary structures in different regimes of plasma confinement on the COMPASS TOKAMAK*, in WDS **14**, 211-214, 2014.

[70] Rabinder N. Madan, *Chua's Circuit: A Paradigm for Chaos*, Vol. 1., World Scientific, 1993.

[71] J. Vandewalle, T. Roska eds., *Proc. of the Special Session on Cellular Neural Networks, ECCTD 1991*, International Journal on Circuit Theory and Applications, **20**(5), 1992.

[72] L. Boncagni, D. Carnevale, A. Cristaldi, S. De Maio, G. Mazzitelli, M. Sassano, V. Vitale, R. Vitelli, and L. Zaccarian, *Temperature control of the FTU Liquid Lithium Limiter*, 2013 European Control Conference, ECC 2013.

[73] L. Ljung, System Indentification: Theory for the User, Prentice Hall, 1999.

[74] F. Battaglia, A. Buscarino, C. Corradino, L. Fortuna, M. Frasca, M.L. Apicella, G. Mazzitelli, *Thermal load analysis and real time hot spots recognition in TOKAMAK using cellular nonlinear networks*, European Conference on Circuit Theory and Design (ECCTD), 2015.

[75] G. Mazzitelli, M.L. Apicella, G. Apruzzese, F. Crescenzi, F. Iannone, G. Maddaluno, V. Pericoli-Ridolfini, S. Roccella, M. Reale, B. Viola, I. Lyublinski, A. Vertkov, and FTU Team, *Experiments on FTU with an actively water cooled liquid lithium limiter* Journal of Nuclear Materials, 463, 1152-1155, 2015.

[76] L. Fortuna, S. Grazian, A. Rizzo, M.G. Xibilia, Soft Sensors for Monitoring and Control of Industrial Processes, *Springer-Verlag*, London, 2006.

[77] L. Fortuna, P. Giannone, S. Graziani, and M.G. Xibilia, *Virtual instruments based on stacked neural networks to improve product*

quality monitoring in a refinery, IEEE Trans. on Instrumentation and Measurement, 56 (1), 2007.

[78] G. Napoli, M.G. Xibilia, *Soft Sensor design for a Topping process in the case of small datasets*, Computers and Chemical Engineering, 35 (11), 2011.

[79] G. Buceti, L. Fortuna, A. Rizzo, M.G. Xibilia, *An Automatic Validation System for Interferometry Density Measurements in the ENEA-FTU TOKAMAK Based on Soft-Computing*, 8th Int. Conf. on Accelerator and Large Experimental Physics Control Systems, ICALEPCS01, San Jose, California, pp. 343-345, 2001.

[80] P. Arena, L. Fortuna, G. Muscato, M.G. Xibilia, Neural Networks in Multidimensional Domains: fundamentals and new trends in modelling and control, Lecture Notes in Control and Information Science, *Springer*, London, 1998.

[81] D. Wroblewski, G. L. Jahns, J. A. Leuer. *TOKAMAK disruption alarm based on a neural network model of the high-beta limit* Nuclear Fusion vol. 37 no. 6 pp. 725, 1997.

[82] A. Vannucci, *Neural Networks Applications to Nuclear Fusion* Physics Institute-University of Sao Paulo, Progress in Electromagnetic Symposium, 2004.

[83] D. F. Valcarcel. et al. *The JET real-time plasma-wall load monitoring system*, Fusion Engineering and Design, 89(3), 243-258, 2014